



# Impact of the Asian monsoon anticyclone on the variability of mid-to-upper tropospheric methane above the Mediterranean Basin

P. Ricaud, B. Sič, L. El Amraoui, Jean-Luc Attié, R. Zbinden, P. Huszar, S. Szopa, J. Parmentier, N. Jaidan, M. Michou, et al.

## ► To cite this version:

P. Ricaud, B. Sič, L. El Amraoui, Jean-Luc Attié, R. Zbinden, et al.. Impact of the Asian monsoon anticyclone on the variability of mid-to-upper tropospheric methane above the Mediterranean Basin. *Atmospheric Chemistry and Physics*, 2014, 14 (20), pp.11427-11446. 10.5194/acp-14-11427-2014 . hal-03045535

**HAL Id: hal-03045535**

**<https://hal.science/hal-03045535>**

Submitted on 10 Dec 2020

**HAL** is a multi-disciplinary open access archive for the deposit and dissemination of scientific research documents, whether they are published or not. The documents may come from teaching and research institutions in France or abroad, or from public or private research centers.

L'archive ouverte pluridisciplinaire **HAL**, est destinée au dépôt et à la diffusion de documents scientifiques de niveau recherche, publiés ou non, émanant des établissements d'enseignement et de recherche français ou étrangers, des laboratoires publics ou privés.



## Impact of the Asian monsoon anticyclone on the variability of mid-to-upper tropospheric methane above the Mediterranean Basin

P. Ricaud<sup>1</sup>, B. Sič<sup>1</sup>, L. El Amraoui<sup>1</sup>, J.-L. Attié<sup>1,2</sup>, R. Zbinden<sup>1</sup>, P. Huszar<sup>3</sup>, S. Szopa<sup>4</sup>, J. Parmentier<sup>1</sup>, N. Jaidan<sup>1</sup>, M. Michou<sup>1</sup>, R. Abida<sup>1</sup>, F. Carminati<sup>1,2,5</sup>, D. Hauglustaine<sup>4,6</sup>, T. August<sup>7</sup>, J. Warner<sup>5</sup>, R. Imasu<sup>8</sup>, N. Saitoh<sup>9</sup>, and V.-H. Peuch<sup>10</sup>

<sup>1</sup>CNRM-GAME, Météo-France/CNRS UMR 3589, Toulouse, France

<sup>2</sup>Université de Toulouse, Laboratoire d'Aérodynamique, CNRS UMR 5560, Toulouse, France

<sup>3</sup>Department of Meteorology and Environment Protection, Faculty of Mathematics and Physics, Charles University, Prague, V Holešovičkách 2, Prague 8, 18000, Czech Republic

<sup>4</sup>Laboratoire des Sciences du Climat et de l'Environnement, CNRS UMR 1572, Gif sur Yvette, France

<sup>5</sup>University of Maryland, College Park, Maryland, USA

<sup>6</sup>Laboratoire Image Ville Environnement, CNRS UMR 7362, Strasbourg, France

<sup>7</sup>EUMETSAT, Darmstadt, Germany

<sup>8</sup>University of Tokyo, Tokyo, Japan

<sup>9</sup>Center for Environmental Remote Sensing, Chiba University, Japan

<sup>10</sup>European Centre for Medium-Range Weather Forecasts, Reading, UK

Correspondence to: P. Ricaud (philippe.ricaud@meteo.fr)

Received: 25 March 2014 – Published in Atmos. Chem. Phys. Discuss.: 17 April 2014

Revised: 16 September 2014 – Accepted: 19 September 2014 – Published: 29 October 2014

**Abstract.** The space and time variabilities of methane (CH<sub>4</sub>) total column and upper tropospheric mixing ratios are analysed above the Mediterranean Basin (MB) as part of the Chemical and Aerosol Mediterranean Experiment (ChArMEx) programme. Since the analysis of the mid-to-upper tropospheric CH<sub>4</sub> distribution from spaceborne sensors and model outputs is challenging, we have adopted a climatological approach and have used a wide variety of data sets. We have combined spaceborne measurements from the Thermal And Near infrared Sensor for carbon Observations – Fourier Transform Spectrometer (TANSO-FTS) instrument on the Greenhouse gases Observing SATellite (GOSAT) satellite, the Atmospheric InfraRed Spectrometer (AIRS) on the AURA platform and the Infrared Atmospheric Sounder Interferometer (IASI) instrument aboard the MetOp-A platform with model results from the Chemical Transport Model (CTM) MOCAGE, and the Chemical Climate Models (CCMs) CNRM-AOCCM and LMDz-OR-INCA (according to different emission scenarios). In order to minimize systematic errors in the spaceborne measurements, we have only considered maritime pixels over the MB. The

period of interest spans from 2008 to 2011 considering satellite and MOCAGE data and, regarding the CCMs, from 2001 to 2010. Although CH<sub>4</sub> is a long-lived tracer with lifetime of ~ 12 years and is supposed to be well mixed in the troposphere, an east–west gradient in CH<sub>4</sub> is observed and modelled in the mid-to-upper troposphere with a maximum in the Western MB in all seasons except in summer when CH<sub>4</sub> accumulates above the Eastern MB. The peak-to-peak amplitude of the east–west seasonal variation in CH<sub>4</sub> above the MB in the upper troposphere (300 hPa) is weak but almost twice as great in the satellite measurements (~ 25 ppbv) as in the model data (~ 15 ppbv). The maximum of CH<sub>4</sub> in summer above the eastern MB can be explained by a series of dynamical processes only occurring in summer. The Asian monsoon traps and uplifts high amounts of CH<sub>4</sub> to the upper troposphere where they build up. The Asian Monsoon Anticyclone redistributes these elevated CH<sub>4</sub> amounts towards North Africa and the Middle East to finally reach and descend in the eastern MB. In the lower troposphere, the CH<sub>4</sub> variability is mainly driven by the local sources of emission in the vicinity of the MB.

## 1 Introduction

During the last decades, the impact and the role that atmospheric trace gases play in climate and air pollution changes have been the source of major concerns. In Intergovernmental Panel on Climate Change (IPCC, 2007), the ongoing changes of our atmosphere (composition, climate, air pollution, radiation) are reported. Among trace gases, methane ( $\text{CH}_4$ ), carbon dioxide ( $\text{CO}_2$ ) and nitrous oxide ( $\text{N}_2\text{O}$ ) are predominant constituents which play an important role in atmospheric changes because they are strongly influenced by human activities. In the frame of predicting the future of the Earth's climate (IPCC, 2007), knowledge of today's  $\text{CO}_2$ ,  $\text{CH}_4$  and  $\text{N}_2\text{O}$  sources and sinks, spatial distribution and time variability is essential and this study will be dedicated to  $\text{CH}_4$ .

The net positive radiative impact of the human activity on climate, starting from 1750, has been evaluated to  $1.6 [+0.6 \text{ to } +2.4] \text{ Wm}^{-2}$  (IPCC, 2007). In the atmosphere, these long-lived greenhouse gases, e.g.  $\text{CH}_4$ ,  $\text{N}_2\text{O}$  and  $\text{CO}_2$ , account for  $2.63 \pm 0.26 \text{ Wm}^{-2}$  and are the predominant radiative terms.  $\text{CO}_2$ , with tropospheric lifetime of 30–95 years, has a radiative efficiency of  $1.4 \times 10^{-5} \text{ Wm}^{-2} \text{ ppb}^{-1}$ , but  $\text{CH}_4$  and  $\text{N}_2\text{O}$ , with tropospheric lifetimes of 12 and 114 years, respectively, are intensely more efficient by  $3.7 \times 10^{-4}$  and  $3.03 \times 10^{-3} \text{ Wm}^{-2} \text{ ppb}^{-1}$ , respectively. IPCC (2007) estimated  $\text{CH}_4$  and  $\text{N}_2\text{O}$  to be responsible for 0.48 [ $+0.43$  to  $0.53$ ] and 0.16 [ $+0.14$  to  $0.18$ ]  $\text{Wm}^{-2}$ , respectively in the radiative forcing changes.

The Mediterranean Basin (MB) is located in a transitional zone between subtropical and mid-latitudes regimes (Lionello, 2012), highly sensitive to climate change. To illustrate, global (or regional) model simulations tend to show a pronounced decrease in precipitation (2000–2100), especially in the warm season (Giorgi and Lionello, 2008), and Lionello (2012) reported on an observed summer west–east asymmetry in precipitation over the MB (1979–2002). In terms of anthropogenic pollution sources, the MB is at the confluence of three continents: Europe, Africa and Asia. The impact of these distinct continental sources such as from industrial and densely populated coastal areas (e.g. Marseille, Barcelona, Athens, Tunis, Cairo, Genoa or Rome) (Kanakidou et al., 2011; Im and Kanakidou, 2012) or forest fires (e.g. in Southeast France, Corsica, Portugal, Greece) (Cristofanelli et al., 2013) is still not perfectly understood, especially on the  $\text{O}_3$  and  $\text{CO}$  budgets in which  $\text{CH}_4$  interplays through complex reactions with nitrogen oxides ( $\text{NO}_x$ ) (Dentener et al., 2005). Besides these regional sources, polluted air masses may originate from Asia during the summer monsoon period (Randel and Park, 2006), Africa through the Hadley cell and upper-level anticyclone (Ziv et al., 2004; Liu et al., 2009) and North America through the westerlies (Christoudias et al., 2012). The Expérience sur Site pour Contraindre les Modèles de Pollution atmosphérique et de Transport d'Emission (ESCOMPTE) campaign (June–

July 2001) aimed to characterize the summer time pollution events in the vicinity of Marseille, France (Cros et al., 2004). The goal of the Mediterranean Intensive Oxidant Study (MI-NOS) campaign (July–August 2001) in the eastern Mediterranean was to measure long-range transport of air pollution and aerosols from Southeast Asia and Europe towards the MB (Ladstätter-Weissenmayer et al., 2003; Scheeren et al., 2003). They have demonstrated the importance of coastal and synoptic transport mechanisms on the variability of constituents but were not adapted to assess the budgets of  $\text{O}_3$ ,  $\text{CO}$  and long-lived species.

The ChArMEx (Chemistry and Aerosol Mediterranean Experiment) Project (<http://charmex.lscce.ipsl.fr/>) is the atmospheric chemistry component of a large multidisciplinary Mediterranean regional programme proposed and conducted by France. It intends, among other objectives, to quantify processes explaining the temporal evolution of chemical compounds and aerosols in the troposphere above the MB. To achieve these goals over the first phase (2010–2015), the programme uses data from satellites, ground-based, sondes, aircraft, models and assimilation in order to evaluate (1) the variabilities and recent trends of several species (e.g.  $\text{O}_3$ ,  $\text{CO}$ ,  $\text{N}_2\text{O}$ ) and aerosols, (2) the synoptic-scale circulation that controls their transport, and (3) the future chemical climate over the MB by 2100.

The past/present nadir-viewing instruments able to actually measure  $\text{CH}_4$  in the troposphere have been/are:

1. the Interferometric Monitor for Greenhouse gases (IMG) instrument operating in the Thermal Infrared (TIR) aboard the ADvanced Earth Observing Satellite (ADEOS-1) platform in 1996–1997 (Clerbaux et al., 1998);
2. the near-IR (NIR) Scanning Imaging Absorption Spectrometer for Atmospheric Chartography (SCIAMACHY) aboard the ENVironment SATellite (ENVISAT) platform (Buchwitz et al., 2000) from 2002 to 2012;
3. the Tropospheric Emission Spectrometer (TES) operating in the TIR aboard the Aura platform (Worden et al., 2012) from 2004 to date;
4. the Thermal And Near infrared Sensor for carbon Observations – Fourier Transform Spectrometer (TANSO-FTS) on the Greenhouse gases Observing SATellite (GOSAT) platform (Yokota et al., 2009) both in the Short-Wave InfraRed (SWIR) and in the TIR from 2008 to date;
5. the Atmospheric InfraRed Sounder (AIRS) aboard the Aqua platform (Xiong et al., 2008) measuring in the TIR from 2004 to date;
6. the Infrared Atmospheric Sounding Interferometer (IASI) instrument aboard the MetOp-A and -B platforms (Hilton et al., 2012) operating in the TIR from

2008 to date, and aboard the MetOp-C platform expected to be launched in 2016.

Table 1 synthesizes the above-mentioned information and shows the nadir-viewing instrument capability to measure tropospheric CH<sub>4</sub>. The sensitivity of the TIR to measure CH<sub>4</sub> is rather weak except on areas showing a high thermal contrast at the surface (vertical gradient of temperature between the surface and the lowermost planetary boundary layer) as the ones encountered over the tropics (Crevoisier et al., 2013) contrarily to the measurements performed in the SWIR (Yoshida et al., 2013). In the NIR, analyses are essentially restricted to areas over land because the retrievals over sea are considered less reliable due to fairly low surface albedo of water, which results in low signals and thus in low signal-to-noise ratios (Georgoulas et al., 2011).

In parallel to the satellite data, models have also been used in order to assess the variability, sources and sinks, and future trends of the long-lived species. Examples are: CH<sub>4</sub> emission and flux estimates at global scales (Bergamaschi et al., 2009; Bousquet et al., 2011), and future evolution of long-lived species included in the international Atmospheric Chemistry and Climate Model Intercomparison Project (ACCMIP) involving more than 10 different models (Lamarque et al., 2013).

Numerous studies have examined the variabilities of atmospheric compounds above the MB to highlight the associated processes (sources and sinks) by coupling surface, balloon-borne, airborne and spaceborne measurements with models' results at different scales, from mesoscales to global scales. Constituents are for instance aerosols (Nabat et al., 2012), radionuclides (Masson et al., 2010), ozone (Liu et al., 2009) and carbon monoxide (Drori et al., 2012). From these references, we note that the impact of (1) the different meteorological regimes and (2) the seasonal variabilities of the emissions of atmospheric constituents, e.g. CO emitted from fires in summers, produces a seasonal variation in all the constituents. It also produces a longitudinal gradient between the eastern MB (EMB) and the western MB (WMB), together with a seasonal variation in the gradient. For example, European anthropogenic emissions were found to significantly influence the EMB surface CO concentrations, while European biomass burning emissions were found to have only a small impact on EMB surface CO concentrations (Drori et al., 2012). Total columns of CH<sub>4</sub> as measured by SCIAMACHY over land and the Eastern Mediterranean from 2003 to 2004 show latitudinal and seasonal variations that cannot be attributed to volcano eruptions (Georgoulas et al., 2011).

The aim of the present paper is to assess the variability of CH<sub>4</sub> in the mid-to-upper troposphere between the EMB and the WMB and to attribute the seasonal variability of the east–west gradient to different processes at both synoptic and global scales depending on the season and the altitude layer considered. We will study in detail the impact of the summer-time long-range transport of CH<sub>4</sub> from Asia to

the EMB through the Asian Monsoon Anticyclone. Since we have already underlined that measurement and modelling of the tropospheric CH<sub>4</sub> distribution are challenging, we will adopt a climatological approach and will use a wide variety of spaceborne measurements and model outputs to verify that they give consistent results.

We have collected the maximum amount of information available from satellite measurements along with model results in order to study the variability of tropospheric CH<sub>4</sub> over the MB and to assess the processes driving this variability. We have thus built a wide data set combining all these pieces of information keeping in mind that (1) it is out of the scope of the present paper to perform a validation of satellite products, (2) all these data sets have their own strengths and weaknesses, and (3) the more data we gather, the better the statistics are and furthermore, the data set consistency can be better assessed. Regarding spaceborne measurements, we have considered tropospheric columns of CH<sub>4</sub> from IASI over the period 2008–2011, and upper tropospheric CH<sub>4</sub> profiles from AIRS and GOSAT over the periods 2008–2011 and March–November 2010, respectively. Regarding the models, we have considered three types of chemical models to calculate CH<sub>4</sub> variability in the mid-to-upper troposphere. The MOCAGE (Josse et al., 2004) chemical transport model (CTM), constrained by the ARPEGE meteorological analyses, is expected to give CH<sub>4</sub> vertical profiles more realistic than climate models over a specified period. Nevertheless, the short spin-up period (3 months vs. 12 years of CH<sub>4</sub> lifetime) used in the MOCAGE runs may impact the CH<sub>4</sub> distribution. On the other hand, chemical climate models (CCMs) such as LMDz-OR-INCA (Hauglustaine et al., 2004; Szopa et al., 2013) from the Laboratoire des Sciences du Climat et de l'Environnement (LSCE) and CNRM-AOCCM (Huszar et al., 2013) from Météo-France are run over a much longer period (greater than 10 years) than MOCAGE and should be better suited to study the climatological variability of CH<sub>4</sub> over the MB. The LMDz-OR-INCA is mainly dedicated to the tropospheric CH<sub>4</sub> profiles since it takes into account the major surface processes that can drive the CH<sub>4</sub> variability in the entire troposphere depending on the inventory scenarios (see Sect. 2.2.3). The CNRM-AOCCM is mainly dedicated to the upper tropospheric–stratospheric CH<sub>4</sub> profiles because it has a detailed description of the stratosphere and should better describe the processes impacting the CH<sub>4</sub> variability in the upper troposphere and lower stratosphere. The three models are thus complementary in the study of the CH<sub>4</sub> variability in the mid-to-upper troposphere over the MB.

The paper is structured as follows. In Sect. 2, we briefly present the spaceborne instruments and data sets involved in this study, namely MetOp-A/IASI, AQUA/AIRS and GOSAT/TANSO, together with the models, namely MOCAGE, CNRM-AOCCM and LMDz-OR-INCA. The meteorology and climatology of CH<sub>4</sub> inferred from the different data sets above the MB are discussed in Sect. 3. The CH<sub>4</sub> variability both in the EMB and the WMB is presented

in Sect. 4. A detailed discussion of the different processes involved in the CH<sub>4</sub> variability above the MB is presented in Sect. 5, underlining the impact of the Asian Monsoon Anticyclone to the distribution of the mid-to-upper CH<sub>4</sub> in the Eastern MB. Finally, Sect. 6 concludes the paper.

## 2 Data sets

### 2.1 Satellite data

Our study analyses CH<sub>4</sub> measurements from three different spaceborne TIR sensors (IASI, AIRS and GOSAT) and consider only the pixels over the Mediterranean Sea due to the larger systematic biases over land. The sensitivity of TIR retrievals strongly depends on surface parameters: emissivity, temperature and thermal contrast (Claeyman et al., 2011). The amplitude of diurnal cycle, and its spatial variability, is larger over land than over the sea. Sea surface temperature exhibits a diurnal amplitude weaker than land surface temperature. Therefore, the vertical sensitivity of the TIR measurements, defined as the full-width at half-maximum of the averaging kernels from the optimal estimation method (Rodgers, 2000), over the sea is consistent during day and night and concentrated in the mid-troposphere. Over the land, the vertical sensitivity is, on average, lower in the middle troposphere during the day than during the night, depending on the actual value of the thermal contrast at the surface.

Infrared sounders' measurement errors can be rather large, e.g. up to 10 % or more for a single CH<sub>4</sub> total column IASI pixel (Turquety et al., 2004). Thus by applying temporal (monthly/seasonally) and geographical averages, including more than a thousand measurements, we can lower the random error to less than 1 %. Systematic errors, if any, will of course be unchanged. For that reason, our analysis relies on a differential method to highlight the CH<sub>4</sub> variability by considering the difference between the EMB and the WMB, assuming that the systematic errors are of the same order of magnitude (although partially unknown) within each geographical box that will be defined in Sect. 3.

#### 2.1.1 The IASI data

IASI, on board of MetOp-A, was launched in 2006 by the European Organisation for the Exploitation of Meteorological Satellites (EUMETSAT). More specifications on platform and instrument can be found on <http://smc.cnes.fr/IASI> and [http://www.eumetsat.int/Home/Main/Satellites/Metop/Instruments/SP\\_2010053151047495](http://www.eumetsat.int/Home/Main/Satellites/Metop/Instruments/SP_2010053151047495). The retrieval algorithm for CH<sub>4</sub> is based on the neural network theory adapted from Turquety et al. (2004). The retrieval method is embedded in the operational IASI level 2 product processing facility at EUMETSAT (EUMETSAT, 2004; Schlüssel et al., 2005; August et al., 2012). From the spectral bandwidth 1230–1347 cm<sup>-1</sup>, the estimated accuracy of the CH<sub>4</sub> total column is about 2 % and the estimated precision is of

the order of 10 % (Turquety et al., 2004). The true accuracy cannot be stated without reference to independent means of comparison, which are not available so far. Consequently, we consider a random Gaussian error of ~ 10 % associated with each single pixel of retrieved total column of CH<sub>4</sub>. At mid-latitudes, the vertical sensitivity of the total column CH<sub>4</sub> is peaking in the mid-troposphere at ~ 8 km from 4 to 14 km (Razavi et al., 2009) and, in the tropics, at ~ 10 km from 5 to 15 km. Geophysical level 2 pre-operational data are provided by EUMETSAT (from version 4 to version 5 from 2008 to 2011). The CH<sub>4</sub> products, not yet validated, are only experimental products, routinely generated for demonstration and evaluation. Note, the number of daily total columns of CH<sub>4</sub> averaged in a 1° × 1° bin is highly variable because of cloud-free IASI considerations. The monthly averaged IASI data within each of the east and west areas defined in Sect. 3 represent an average of 30 000–70 000 pixels depending on the month considered.

#### 2.1.2 The AIRS data

AIRS is onboard the space platform NASA EOS Aqua, launched in 2002 (<http://airs.jpl.nasa.gov/>). AIRS measures approximately 200 channels in the 7.66 µm absorption band of CH<sub>4</sub>, of which 71 channels are used to retrieve CH<sub>4</sub>. A detailed description of the retrieval algorithm can be found in Susskind et al. (2011). Note, the averaging kernels provided by NASA will be considered further (Sect. 4.2) in order to degrade the vertical resolution of the model outputs. At mid-latitudes, the most sensitive layer of AIRS channels to CH<sub>4</sub> is at 300 hPa (~ 9 km) with a vertical sensitivity from 700 to 100 hPa (Xiong et al., 2008), and, in the tropics, at 200 hPa from 500 to 70 hPa consistently with the IASI TIR measurement sensitivity. Around 200–300 hPa, considering the version V5 used in the present analysis (Xiong et al., 2008), the precision of AIRS CH<sub>4</sub> is estimated to be 30 ppbv (1.7 %) and validation using in situ aircraft measurements shows that the accuracy of the retrieved CH<sub>4</sub> is 0.5–1.6 %. Daily maritime profiles of CH<sub>4</sub> have been averaged in 1° × 1° bins over the MB. The monthly-averaged AIRS data within each of the east and west areas defined in Sect. 3 represent an average of 6000–10 000 vertical profiles depending on the month considered.

#### 2.1.3 The GOSAT data

The Japanese Aerospace Exploration agency (JAXA) launched the GOSAT platform in 2009, with the TANSO-FTS spectrometer, a nadir-viewing instrument designed for greenhouse gases research, CO<sub>2</sub> and CH<sub>4</sub>, operating in the TIR and SWIR domains [0.7–14.3 µm] (Kuze et al., 2009). More specifications on platform and instrument can be found on <http://www.gosat.nies.go.jp/>. The sensitivity of the SWIR CH<sub>4</sub> measurements at 1.67 µm (Yokota et al., 2009) at mid-latitudes over the sea is very weak, thus few meaningful

**Table 1.** Nadir-viewing instruments having the capabilities to measure CH<sub>4</sub> in the troposphere. Please, refer to the text for the acronyms.

Platform	Instrument	Operation time	Wavelength	References
ADEOS-1	IMG	1996–1997	TIR	Clerbaux et al. (1998)
ENVISAT	SCIAMACHY	2002–2012	NIR	Buchwitz et al. (2000)
Aura	TES	2004–date	TIR	Worden et al. (2012)
GOSAT	TANSO-FTS	2008–date	SWIR & TIR	Yokota et al. (2009)
Aqua	AIRS	2004–date	TIR	Xiong et al. (2008)
MetOp-A	IASI	2008–date	TIR	Hilton et al. (2012)
MetOp-B	IASI	2012–date	TIR	Hilton et al. (2012)
MetOp-C	IASI	Expected in 2016	TIR	Hilton et al. (2012)

pixels could have been retrieved, preventing the use of such information in our analysis. The TIR measurements from Band 4 (5.5–4.3  $\mu\text{m}$ ) provide vertical profiles of CH<sub>4</sub> along seven vertical levels (Imasu et al., 2007) by using the optimal estimation method with a vertical sensitivity in the tropics peaking at 10 km (higher than at mid-latitudes) from 5 to 15 km (Saitoh et al., 2012), consistently with the vertical sensitivity of IASI (Razavi et al., 2009) and AIRS (Xiong et al., 2008) in the tropics. A selection by using Degree of Freedom of Signal (DFS) is applied for the data having DFS values larger than 0.6 for CH<sub>4</sub>. TIR data (L2 Version 0.10) were only available from 16 March to 24 November 2010 from the GOSAT User Interface Gateway at the time the analysis was performed. These retrievals provide vertical profiles of mixing ratio of CH<sub>4</sub> from 1000 to 100 hPa. Comparisons with aircraft measurements show that the average difference between the GOSAT (TIR) and aircraft CH<sub>4</sub> values (TIR – aircraft) is –5 ppbv, and the  $1\sigma$  standard deviation is 15 ppbv (Saitoh et al., 2012). Daily maritime profiles of CH<sub>4</sub> have been averaged in  $1^\circ \times 1^\circ$  bins over the MB. The monthly averaged GOSAT data within each of the east and west areas defined in Sect. 3 represent an average of 100–300 vertical profiles depending on the month considered, namely 20–30 times less than for AIRS.

## 2.2 The model data

### 2.2.1 The MOCAGE data

MOCAGE (MOdèle de Chimie Atmosphérique à Grande Echelle) (Peuch et al., 1999) is a 3-D CTM which covers the planetary boundary layer, the free troposphere and the stratosphere for different applications such as: operational chemical weather forecasting (Dufour et al., 2005); tropospheric and stratospheric research studies (Claeyman et al., 2010; Ricaud et al., 2009); and data assimilation research (El Amraoui et al., 2010; Claeyman et al., 2011). In our study, MOCAGE is forced dynamically by wind and temperature fields from the analyses of the ARPEGE model (Courtier et al., 1991). The MOCAGE horizontal resolution is  $2^\circ \times 2^\circ$  and the model uses a semi-Lagrangian transport scheme. It includes 47 levels from the surface up to 5 hPa with a ver-

tical resolution of about 800 m around the tropopause, 400–800 m in the troposphere and 40–400 m in the seven levels of the boundary layer. Chemistry used within MOCAGE is a combination of tropospheric (RACM described in Stockwell et al., 1997) and stratospheric (REPROBUS described in Lefèvre et al., 1994) chemical schemes. Initial chemical conditions are taken from climatological fields over a spin-up period of 3 months allowing the model to quickly bring chemical fields to realistic spatial distributions. Surface emissions prescribed in MOCAGE are based upon yearly or monthly averaged climatologies. More precisely, the CH<sub>4</sub> surface emissions are monthly averages and split into anthropogenic sources taken from the Intergovernmental Panel on Climate Change (IPCC) (Dentener et al., 2005), biomass burning (van der Werf et al., 2003) and biogenic sources (Michou and Peuch, 2002). The CH<sub>4</sub> climatologies are representative of year 2000 for a total emission rate of 534 Tg(CH<sub>4</sub>) yr<sup>–1</sup>.

### 2.2.2 The CNRM-AOCCM data

The atmospheric model embedded in CNRM-AOCCM is presented in Huszar et al. (2013) based on the Atmosphere–Ocean General Circulation Model (AOGCM) CNRM-CM5 described in Voldoire et al. (2013). The main difference between CNRM-CM5 and CNRM-AOCCM resides in the “on-line” coupling with a stratospheric chemistry which is based on the REPROBUS scheme. This scheme is applied on the whole vertical column, except between the surface and the 560 hPa level where long-lived chemical species are relaxed towards global average surface value following the A1B scenario from IPCC (2007). The A1B scenario mainly describes a future world of very rapid economic growth, global population that peaks in mid-century and declines thereafter, and the rapid introduction of new and more efficient technologies. Convection of species is not considered. In this chemistry version, the 3-D distribution of the seven absorbing gases (H<sub>2</sub>O, CO<sub>2</sub>, O<sub>3</sub>, CH<sub>4</sub>, N<sub>2</sub>O, CFC11 and CFC12) is then provided by the chemistry module of CNRM-AOCCM and interacts with the radiative calculations. More details can be found in Michou et al. (2011). In the present version, there are about 50 chemical species, and the horizontal resolution is  $2.8^\circ \times 2.8^\circ$ . Distribution of atmospheric constituents at the

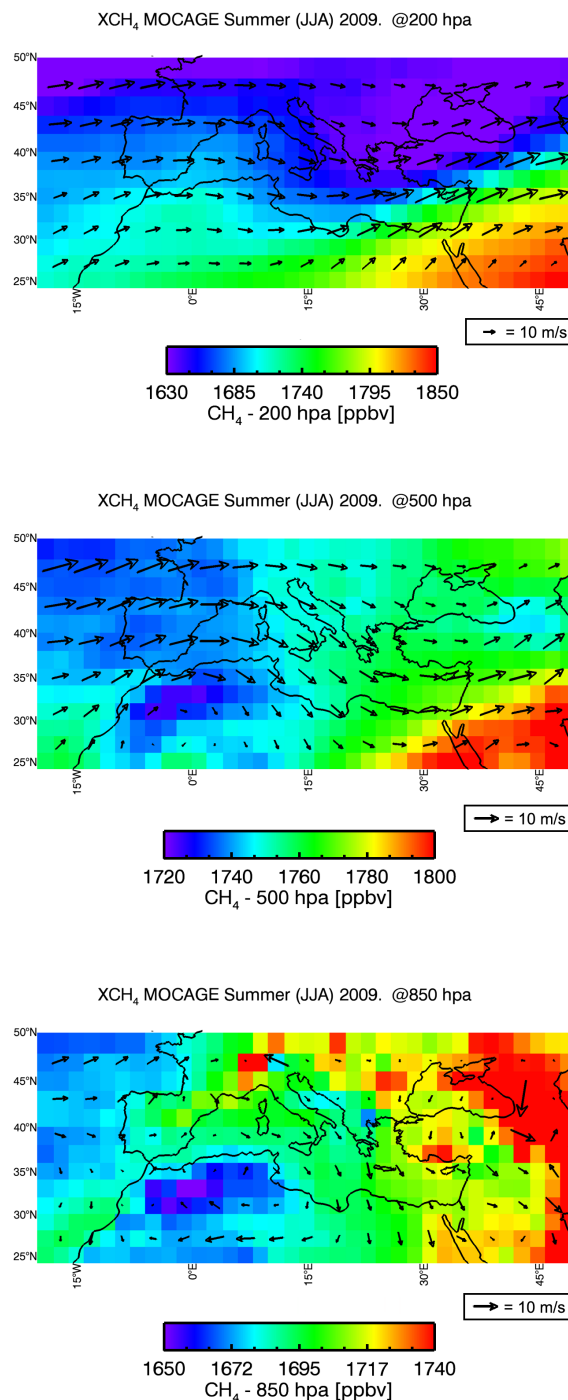
surface are zonally symmetric below 500 hPa (Fig. 10) and greenhouse gases follow the A1B scenario on atmospheric chemistry and climate for the period of 1940–2100. In the present analysis, for this model, we only consider the climatological period 2001–2010.

### 2.2.3 The LMDz-OR-INCA data

The Interaction between Chemistry and Aerosol (INCA) model is used to simulate the distribution of aerosols and gaseous reactive species in the troposphere. In the present configuration, the model includes 19 hybrid vertical levels extending up to 4 hPa, and a horizontal resolution of  $1.9^\circ$  in latitude and  $3.75^\circ$  in longitude. INCA is coupled online to the LMDz General Circulation Model (GCM) to account, with different degrees of complexity, for climate chemistry interactions. In the simulations described here, LMDz is coupled with the ORCHIDEE (Organizing Carbon and Hydrology in Dynamic Ecosystems) dynamic global vegetation model (Krinner et al., 2005) for soil/atmosphere exchanges of water and energy (Hourdin et al., 2006), but not for biogenic  $\text{CO}_2$  or Volatile Organic Compounds (VOCs) fluxes. Together, these three models form the LMDz-OR-INCA model. Fundamentals for the gas phase chemistry are presented in Hauglustaine et al. (2004) and first results with the full tropospheric gaseous chemical scheme are presented by Folberth et al. (2006). The model includes 223 homogeneous chemical reactions, 43 photolytic reactions and 6 heterogeneous reactions including non-methane hydrocarbon oxidation pathways and aerosol formation. The LMDz-OR-INCA simulation covers four future projections of emissions for the 2000–2100 period. The Representative Concentration Pathways (RCP) emissions are used (Lamarque et al., 2011). They correspond to emission trajectories compatible with the evolution of radiative forcing equivalent in 2100 to 2.6, 4.5, 6.0 and  $8.5 \text{ Wm}^{-2}$  relative to pre-industrial values (labelled therein after RCP 2.6, 4.5, 6.0 and 8.5). In the present analysis, for this model, we only consider the climatological period 2001–2010.

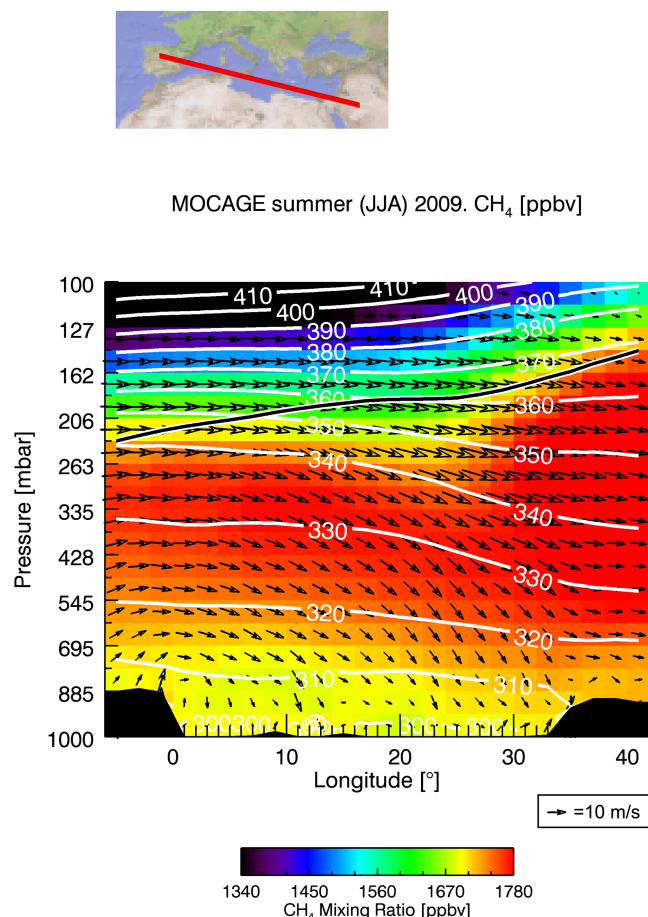
### 3 Atmospheric conditions controlling the spatial distribution of methane

Figure 1 shows the  $\text{CH}_4$  fields calculated by MOCAGE for summer (June–July–August, JJA) 2009 over the MB at 850, 500 and 200 hPa, superimposed with the wind fields from the ARPEGE analyses averaged over the same period. Figure 2 presents the  $\text{CH}_4$  vertical distribution as calculated by MOCAGE in summer 2009 along an east–west axis above the MB. Similarly to Figs. 1 and 2, Figs. 3 and 4 present, for winter (December–January–February, DJF) 2009, the  $\text{CH}_4$  fields as calculated by MOCAGE over the MB at 850, 500 and 200 hPa, and along an east–west axis, respectively. In Figs. 2 and 4, the MOCAGE  $\text{CH}_4$  fields are



**Figure 1.** From bottom to top: fields of  $\text{CH}_4$  as calculated by MOCAGE and averaged for summer (JJA) 2009 at 850, 500 and 200 hPa. Superimposed are the horizontal winds from ARPEGE averaged over the same period. In order to highlight the  $\text{CH}_4$  horizontal gradients, the range of the colour scale changes from top to bottom.





**Figure 2.** Vertical distribution of  $\text{CH}_4$  as calculated by MOCAGE and averaged for JJA 2009 as a function of longitude along the red line represented above the figure. Superimposed are the associated longitudinal and vertical winds from ARPEGE, together with the isentropes (white lines) and the cold point tropopause from NCEP/NCAR reanalyses (black line) averaged over the same period.

superimposed with (1) the wind fields from ARPEGE analyses and (2) the cold point tropopause pressure fields provided by the National Centers for Environmental Prediction (NCEP)/National Center for Atmospheric Research (NCAR) reanalyses, all these data being averaged over the same period.

Considering the meteorology of the MB, we observe two different regimes. (1) In winter (Fig. 3), and more generally from autumn to spring (not shown), from the boundary layer to the upper troposphere, air masses are essentially coming from either Europe or Eastern Atlantic Ocean. (2) In summer (Fig. 1), the meteorology of EMB and WMB is more complex and depends on the altitude considered.

In the planetary boundary layer in summer (Fig. 1, bottom), cells develop in the WMB, and air masses come from Europe, northern Africa and the eastern Atlantic Ocean, whilst in the EMB, air masses originate from four ma-

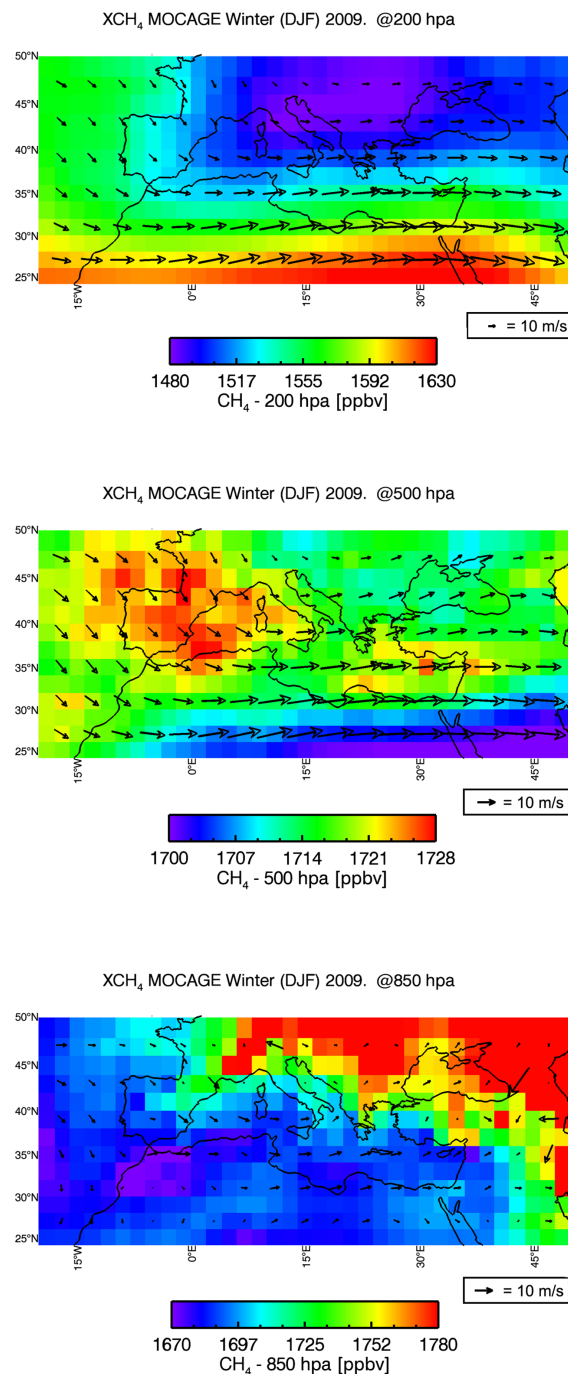


**Figure 3.** As Fig. 1, but for winter (DJF) 2009.

for source regions: (i) long fetch of maritime European air masses from the northwest throughout the year, (ii) north-east continental flow originating in southeastern Europe (Etesian winds) in summer, (iii) southeast flow from the Arabian Peninsula occurring in the fall, and (iv) southwest flow along the North African coast most frequent during late winter and spring (Dayan, 1986). In the middle troposphere (Figs. 1 and 3, middle), whatever the season, air masses are essentially



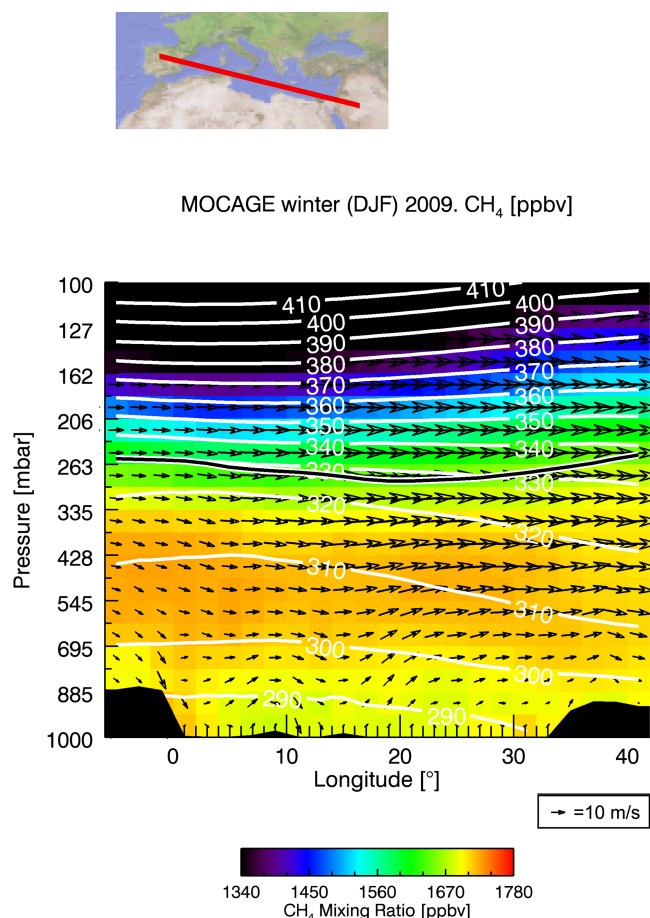


**Figure 4.** As Fig. 2, but for winter (DJF) 2009.

coming from the west for both parts of the basin. In summer (Fig. 1, top), upper tropospheric air masses in the WMB are essentially coming from the west, but in the EMB, they also originate in northern Africa and the Arabian Peninsula (Ziv et al., 2004; Liu et al., 2009), and even farther away, from Asia (we will discuss this point in Sects. 4 and 5). Note that, in summer, the EMB and WMB are also affected by the location of the descending branch of the Hadley cell (Fig. 2). These summer climatologies are all consistent with Millán et al. (1997), Lelieveld et al. (2002), Ziv et al. (2004) and Schicker et al. (2010).

Seasonally averaged wind fields from ARPEGE analyses show two different regimes in the surface pressure values during the summer (Fig. 1, bottom) and the winter (Fig. 3, bottom) periods. During the summer in the WMB, there is a higher pressure regime than in the EMB (Fig. 1, bottom). In the lowermost troposphere (850 hPa), an anticyclonic cell develops in the WMB that has an impact on the distribution of  $\text{CH}_4$  by producing a local minimum (Fig. 1, bottom). At 850 hPa, air masses are coming from Europe, North Africa and the Atlantic Ocean. The  $\text{CH}_4$  distribution shows a maximum over Europe, consistently with the strongest emission

zones (Fig. 10), and a strong minimum over North Africa. In the mid-troposphere (500 hPa), air masses are coming from Europe, and the Atlantic Ocean (Fig. 1, middle). An east–west gradient is detected with more  $\text{CH}_4$  on the EMB. In the upper troposphere (200 hPa) (Fig. 1, top), air masses originate from the Atlantic Ocean (even North America) and from North Africa and Asia producing over the MB an obvious north–south gradient with more  $\text{CH}_4$  in the south (upper troposphere) than in the north (lower stratosphere) attributed to the impact of long-range transport of pollutants (as discussed in Sect. 5). A systematic subsidence is present over the MB (Fig. 2) whatever the longitudinal bin considered due to the presence of semi-permanent subtropical high pressure systems which are centred over the tropical deserts. More precisely, in the WMB, the descent is caused by the presence of a high-pressure cell (Fig. 1, bottom) whilst, in the EMB, it is coming from the Hadley cell that is further displaced over the Northern Africa producing a downward branch in the area 30–35° N. The tropopause moves up from  $\sim 200$  hPa in the WMB to  $\sim 175$  hPa in the EMB (Fig. 2). The  $\text{CH}_4$  distribution shows (1) an obvious transition at the tropopause and (2) a minimum in the west and a maximum in the east in the low troposphere accentuated by the systematic descent in the EMB that brings  $\text{CH}_4$ -enriched air masses from the upper troposphere to the mid-to-low troposphere.

In winter, the meteorological condition of the MB is much more homogeneous with westerlies blowing whatever the pressure considered from 850 to 200 hPa (Figs. 3–4). North–south (and to a lesser extent east–west) gradients in  $\text{CH}_4$  can also be detected (Fig. 3) associated with the local sources of emission over Europe at 850 hPa and with the stratosphere/troposphere transition at 200 hPa. The 500 hPa layer is a transition region between the low and the upper troposphere with minima of  $\text{CH}_4$  over North Africa and a cell of high  $\text{CH}_4$  in the WMB (Fig. 3, middle). Contrarily to summer, since the temperature of the Mediterranean Sea is greater than that of the surrounding continents, a systematic upward motion is present (Fig. 4) whatever the longitudinal bin considered. The Hadley cell is further displaced to the south (latitude  $< 30^\circ$  N) and its downward branch does not affect significantly the EMB. The tropopause pressure is rather stable from the WMB to the EMB, around 260 hPa. The  $\text{CH}_4$  distribution shows minimum in the lowermost troposphere and a maximum in the middle troposphere (Fig. 4).

## 4 $\text{CH}_4$ variability

### 4.1 $\text{CH}_4$ spatial distribution of the MB

Figure 5 shows the distributions of (1) the  $\text{CH}_4$  total columns from IASI over the MB averaged in summer 2009 to compare with the MOCAGE results in time coincidence, and (2) the  $\text{CH}_4$  mixing ratios from AIRS at 260 hPa over the MB averaged in summer 2009 to compare with the MOCAGE results

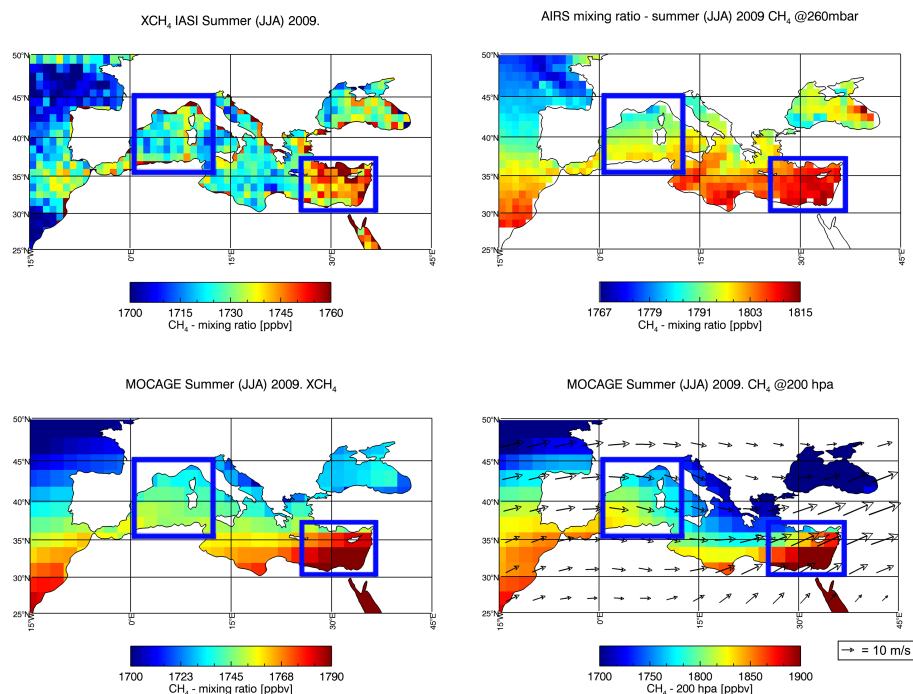


**Figure 5.** Field of total columns of  $\text{CH}_4$  as measured by IASI and averaged for summer (JJA) 2009 (top left), and field of  $\text{CH}_4$  at 260 hPa as measured by AIRS and averaged for JJA 2009 (top right). (Bottom) Same as above but as calculated by MOCAGE. Satellite data are represented in a  $1^\circ \times 1^\circ$  resolution whilst model data are shown in a  $2^\circ \times 2^\circ$  resolution. The two blue squares in the lower left panel represent the WMB and EMB where the measured and modelled data are selected over the Mediterranean Sea. Superimposed are the horizontal winds from ARPEGE at 200 hPa averaged over the same period (bottom right). In order to highlight the  $\text{CH}_4$  horizontal gradients, the range of the colour scale changes for each panel.

at 200 hPa in time coincidence. The measured and modelled data are selected only for the maritime pixels within the boxes  $[36\text{--}45^\circ \text{ N}, 1\text{--}12^\circ \text{ E}]$  and  $[30\text{--}37^\circ \text{ N}, 26\text{--}37^\circ \text{ E}]$  to represent the WMB and the EMB (blue squares in each figure), respectively.

Due to its long lifetime ( $\sim 12$  years),  $\text{CH}_4$  is considered as a well-mixed species in the troposphere. Nevertheless, the  $\text{CH}_4$  spatial distribution over the MB in summer (JJA) 2009 shows some gradients both in the east–west and the north–south directions. Indeed, in the middle troposphere (inferred from the sensitivity of the IASI total columns) and in the upper troposphere (200–260 hPa), an east–west gradient is observed in the model and satellite data of  $\sim 60$  ppbv ( $\sim 4\%$ ) in total column and  $\sim 30\text{--}150$  ppbv ( $\sim 2\text{--}9\%$ ) in mixing ratio. A north–south gradient is also detected in the MOCAGE and AIRS data but not in the IASI data set. Therefore, there is systematically a maximum of  $\text{CH}_4$  from the middle to the upper troposphere in the EMB compared to the WMB. In the mid-to-upper troposphere, these east–west gradients do not originate from the  $\text{CH}_4$  sources which are more intense in Europe than in northern Africa or in central Asia (Fig. 1) but rather from the long-range transport of Asian-origin air masses and the subsidence of air masses in the EMB (Figs. 1 and 2 and detailed discussion in Sect. 5).

Quantitatively, there is a positive bias in MOCAGE vs. IASI of less than 30 ppbv (2 %) in  $\text{CH}_4$  total column mixing ratio. The east–west gradient is consistent between IASI and MOCAGE but the north–south modelled gradient is not detected in the IASI data set. In the upper troposphere (200–260 hPa), MOCAGE and AIRS  $\text{CH}_4$  mixing ratios are very consistent with gradients more accentuated in the model ( $\sim 150$  ppbv) than in the AIRS data sets ( $\sim 30$  ppbv). A systematic negative bias of MOCAGE compared to AIRS of  $\sim 100$  ppbv up to 150 ppbv (10 %) in the northern MB is detected. We discuss in the next section the consistency of the vertical profiles of  $\text{CH}_4$  measured by the different spaceborne sensors and calculated by MOCAGE together with the associated biases.

## 4.2 Vertical profiles

Figure 6 shows the vertical profiles of  $\text{CH}_4$  as measured by AIRS (750–100 hPa) and GOSAT (1000–100 hPa) and as calculated by MOCAGE (1000–100 hPa) averaged over the EMB and the WMB depending on the four seasons: winter (DJF), spring (March–April–May, MAM), summer (JJA) and autumn (September–October–November, SON) 2010. There is a good agreement to within 20–30 ppbv between AIRS and GOSAT data in the vertical domain 750–200 hPa. GOSAT

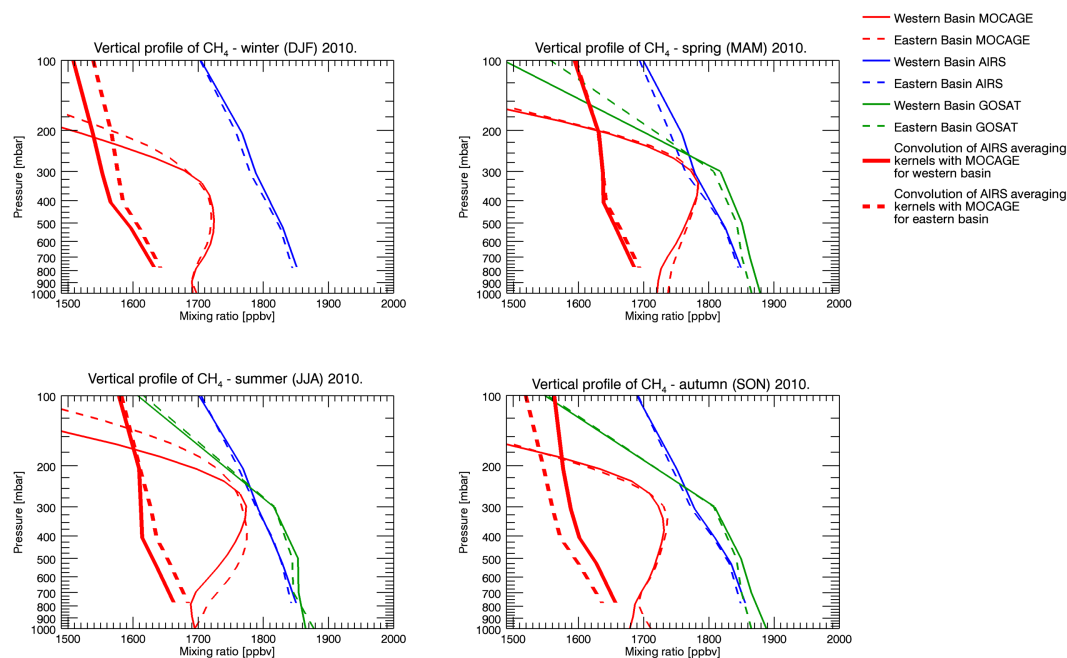


**Figure 6.** From top to bottom and from left to right: seasonally averaged vertical profiles of  $\text{CH}_4$  as measured by AIRS (blue lines) and GOSAT (green lines), and as calculated by MOCAGE (thin red lines) over the Eastern (dashed lines) and Western (solid lines) MBs in winter, summer, spring and autumn 2010. Also shown are the seasonally averaged MOCAGE profiles convolved with the AIRS averaging kernels (thick red lines) for the four seasons over the EMB (dashed lines) and WMB (solid lines).

is systematically greater than AIRS by about 20–30 ppbv for pressure greater than 300 hPa, whilst for pressure less than 300 hPa, AIRS is systematically greater than GOSAT by 20 ppbv degrading to 50–200 ppbv at 100 hPa. But the shape of the vertical spaceborne profiles is consistent between AIRS and GOSAT. Separately, whatever the season considered, the MOCAGE low-to-mid tropospheric  $\text{CH}_4$  is low biased compared to the measured profiles by  $\sim 150$ –200 ppbv. Furthermore, the MOCAGE vertical profiles systematically show a maximum at 300 hPa, which is not present in any of the spaceborne measurements, and a strong decrease above.

In order to assess the impact of the vertical sensitivity of the spaceborne measurements to the  $\text{CH}_4$  profiles, we have applied the AIRS averaging kernels, derived from the AIRS retrieval method (Susskind et al., 2011) and provided by NASA for each AIRS pixel, to the profiles calculated by MOCAGE. Note that the AIRS a priori vertical profiles are not used in our study since we are only interested in the vertical shape of the  $\text{CH}_4$  profile and not the absolute amount of  $\text{CH}_4$ . Degrading the vertical resolution of the MOCAGE profiles by the convolution of averaging kernels (Fig. 6) shows a strong impact on the vertical shape of the  $\text{CH}_4$  profiles since the strong maximum at 300 hPa is no longer present. Convolved MOCAGE  $\text{CH}_4$  profiles are now consistent with AIRS  $\text{CH}_4$  profiles whatever the season considered but a systematic low bias of  $\sim 150$ –200 ppbv (8–10 %) between AIRS and MOCAGE convolved profiles is observed. This might be

due to the fact that no a priori information contributes to the convolved profile. This is also due to the overall underestimation of  $\text{CH}_4$  by global models. Indeed, due to coarse horizontal resolution and large uncertainties in the estimated surface emissions, tropospheric  $\text{CH}_4$  lifetimes, e.g. evaluated by the multi-model intercomparison project ACCMIP, are about 5–13 % lower than observation estimates (Naik et al., 2013; Voulgarakis et al., 2013).

It is almost impossible to validate the spaceborne vertical profiles with an external data set since, even within the Total Carbon Column Observing Network (<http://www.tccon.caltech.edu/>) giving accurate and precise column-averaged abundances of  $\text{CH}_4$  (Wunch et al., 2010), no measurement sites are unfortunately available in the vicinity of the MB. Near the surface, the amount of  $\text{CH}_4$  is about 1700–1750 ppbv for MOCAGE, and is on average less than the  $\text{CH}_4$  GOSAT data by about 150–200 ppbv. At this stage, it is worthwhile considering surface data within the MB. The NOAA Earth System Research Laboratory (ESRL) In Situ Methane Measurements provide some surface  $\text{CH}_4$  measurements within and/or in the vicinity of the MB: Lampedusa, Italy (35.52° N, 12.62° E, 45 a.m.s.l.), Centro de Investigacion de la Baja Atmosfera (CIBA), Spain (41.81° N, 4.93° W, 845 a.m.s.l.) and Negev Desert, Israel (30.86° N, 34.78° E, 477 a.m.s.l.). On average, these three sites indicate (not shown) a surface  $\text{CH}_4$  annual mean of about 1875 ppbv in 2010, with an annual oscillation of  $\sim 20$  ppbv amplitude. Consequently, the amount of surface  $\text{CH}_4$  in the MOCAGE

run for 2010 is actually low biased by about 150–200 ppbv (8–10 %) but is very consistent with the LMDz-OR-INCA surface data of  $\sim 1725$ – $1750$  ppbv over the Mediterranean (Fig. 10). The slight differences between the EMB and the WMB according to the season and height are studied in detail in the next section.

#### 4.3 The east–west seasonal variations: measured and calculated differences

The seasonal variations of the differences in  $\text{CH}_4$  fields between the EMB and the WMB (i.e. EMB minus WMB, labelled as “E–W” in what follows) as measured by AIRS, GOSAT and IASI and as calculated by LMDz-OR-INCA, CNRM-AOCCM and MOCAGE are presented in Fig. 7 when considering the upper troposphere (AIRS, GOSAT, LMDz-OR-INCA and CNRM-AOCCM at 260 and 300 hPa) and the middle troposphere (IASI and MOCAGE total column mixing ratios). In the middle and upper troposphere (Fig. 7), despite the fact that spaceborne measurements and modelling of  $\text{CH}_4$  are challenging, the modelled and measured seasonal variations of E–W are consistent to each other showing a maximum (peak) in summer and a wide minimum in winter.

If we consider the time evolution of the total column mixing ratios (namely focusing on the middle troposphere), we note that both MOCAGE and IASI show a maximum in summer, although 3 times greater in MOCAGE ( $\sim 60$  ppbv) than in IASI ( $\sim 20$  ppbv) in July and August. The minimum in January–February is close to zero but slightly positive in October (5–10 ppbv). The much stronger maximum in August calculated by MOCAGE compared to IASI  $\text{CH}_4$  total columns might be attributable to the sensitivity of spaceborne measurements in the middle troposphere whilst the MOCAGE tropospheric columns cover the entire troposphere from the surface to the top of the model atmosphere, namely 5 hPa.

In the upper troposphere (300 hPa), the spaceborne instrument data sets show an E–W maximum in summer of  $\sim 12$  ppbv in August for AIRS and an E–W wide maximum of  $\sim 5$  ppbv in July–September for GOSAT. An E–W peak of  $\sim 10$  ppbv in July–August is also calculated by CNRM-AOCCM although, in the LMDz-OR-INCA data set, the E–W maximum is slightly positive in August ( $\sim 2$  ppbv). The minimum in the satellite data sets is observed in March–April and is negative (from  $-15$  to  $-20$  ppbv) consistently with the LMDz-OR-INCA data set whilst the CNRM-AOCCM E–W minimum is less intense ( $-6$  ppbv in February and April). The peak-to-peak amplitude of the E–W seasonal variation is almost twice as great in the satellite measurements ( $\sim 25$  ppbv) as in the model data ( $\sim 15$  ppbv). This represents a  $\sim 1.5$ – $2.0$  % variation of  $\text{CH}_4$  in the E–W over the entire year. These results suggest that the difference in amplitude between satellite and model in the seasonal evolution of E–W may be due to: (a) the comparison technique,

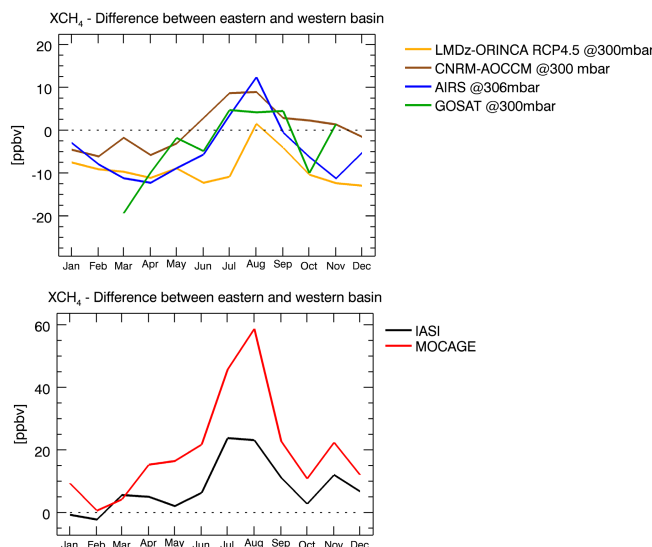


**Figure 7.** Top: seasonal evolution of the difference in the  $\text{CH}_4$  fields between the Eastern and Western MB as measured by AIRS (blue line) and GOSAT (green line) at 306 and 300 hPa, respectively and as calculated by LMDz-OR-INCA (yellow line) and CNRM-AOCCM (brown line). Bottom: seasonal evolution of the difference in the  $\text{CH}_4$  total columns between the Eastern and Western MB as measured by IASI (black line) and as calculated by MOCAGE (red line). The LMDz-OR-INCA and CNRM-AOCCM data sets cover the climatological period 2001–2010. The MOCAGE and IASI data sets cover the period 2008–2011 whilst the satellite AIRS and GOSAT data sets are representative of the year 2010.

the vertical resolution of the models is much better than the vertical resolution of the satellite observations; (b) regarding the processes in summer, we may have less  $\text{CH}_4$  trapped in the Asian Monsoon Anticyclone redistributed towards the EMB (see Sect. 5) in the models compared to the measurements; (c) regarding the processes in winter, since westerlies are mainly present over the MB in the mid-to-upper troposphere (Figs. 3 and 8), we may have too much and/or too rapidly  $\text{CH}_4$  transported over the Mediterranean Sea to the east compared to the west, leading to a too smooth E–W gradient in the models compared to the measurements.

Recall that statistically the number of spaceborne measurements used in our analysis (see Sect. 2) is  $\sim 5$  times greater in IASI compared to AIRS, and  $\sim 30$  times greater in AIRS compared to GOSAT. Consequently, GOSAT monthly averaged data appear noisier than AIRS monthly averaged data. Note that IASI total columns are not and cannot be directly compared with AIRS or GOSAT profiles in our analysis. Nevertheless, although IASI data are not operationally produced, the IASI E–W seasonal variation is very consistent with the E–W seasonal variation as deduced from all other data sets. The monthly random error attributed to the E–W IASI  $\text{CH}_4$  is about 0.1 %, much less than the observed peak-to-peak yearly variation. We estimate that the AIRS monthly random error attributed to the E–W  $\text{CH}_4$  is twice as great as



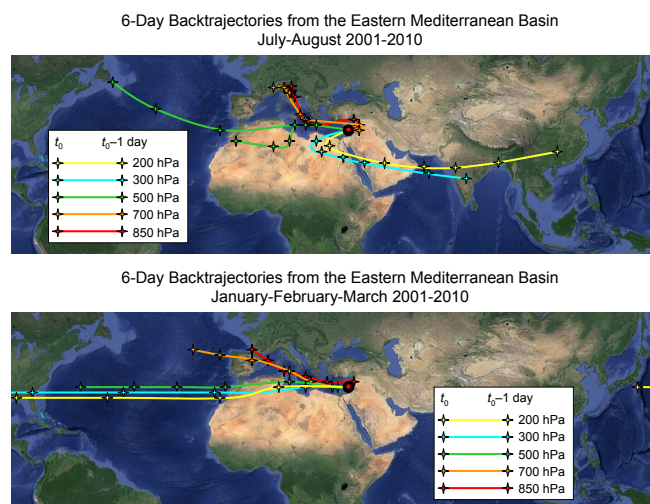


**Figure 8.** Top: climatological six-day back trajectories from the point at 33° N, 35° E located in the EMB (red filled circle) calculated from the British Atmospheric Data Centre trajectory service (<http://badc.nerc.ac.uk/community/trajectory/>) from 1 July to 31 August from 2001 to 2010 every 12 h at 850 (red line), 700 (orange line), 500 (green line), 300 (blue line) and 200 hPa (yellow line). The position of the gravity centre of each distribution at each level is represented every 24 h by a star. Bottom: same as top, but calculated from 1 January to 31 March 2001–2010.

the one calculated for IASI, and that the GOSAT monthly random error is about 5 times greater than the ones calculated for IASI. We discuss in the next section the origin of the summer peak in the E–W seasonal variation.

## 5 Contribution of the Asian monsoon anticyclone

As stated in Sects. 3 and 4, interpretation of the E–W CH<sub>4</sub> seasonal variation along the vertical requires consideration of the distribution of CH<sub>4</sub> over the Asian continent because of the importance of long-range transport. From Rodwell and Hoskins (1996), it is known that there is a meteorological link between monsoons and the dynamics of the deserts and more precisely between the Asian monsoon and the EMB summer regime. The subsidence centre over the EMB owes its location, timing of onset and intensity to the Asian monsoon, and not to the Hadley circulation. Although it takes less than 1 day to reach the upper troposphere within the Asian monsoon, back trajectory calculation (Ziv et al., 2004) shows that it takes about 3–4 days for an air parcel to reach and descend the upper tropospheric EMB from the vicinity of the anticyclone that develops over the Asian monsoon. Inside the Asian Monsoon Anticyclone (AMA), pollutants like CO originating from the surface constitute about 50 % of the CO concentration at 100 hPa (Park et al., 2009), with the reminder resulting from chemical production in the troposphere. Most of the CO within the AMA comes from In-

dia and South East Asia, with an insignificant contribution from the Tibetan Plateau. Randel and Park (2006), and Park et al. (2009) have analysed in detail this phenomenon over Asia by considering dynamical parameters (potential vorticity) and chemical species (H<sub>2</sub>O, CO and O<sub>3</sub>).

Numerous studies have already evaluated the impact of transport vs. emission of pollutants and aerosols over the MB and its temporal variability considering different pollutants, chemical compounds and aerosols (Wanger et al., 2000; Lelieveld et al., 2002; Pfister et al., 2004; Kallos et al., 2007). As stated in Sect. 3, two main dynamic factors affect the EMB: (1) the upper to mid-tropospheric subsidence, and (2) the lower-level cool Etesian winds (Ziv et al., 2004). Although the EMB is characterized by strong descent in the middle and upper troposphere in summer, transport from the boundary layer accounts for about 25 % of the local Middle Eastern contribution to the ozone enhancement in the middle troposphere (Liu et al., 2009). Elevated CO episodes in EMB during summer can also be attributed to synoptic conditions prone to favourable transport from Turkey and eastern Europe towards the EMB rather than increased emissions (Drori et al., 2012). Upper tropospheric longitudinal gradients in the EMB of CH<sub>4</sub>, CO, hydrocarbons, including acetone, methanol, and acetonitrile, halocarbons, O<sub>3</sub> and total reactive nitrogen (NO<sub>y</sub>) were also attributed in August 2001 to the chemical impact of the Asian plume (Scheeren et al., 2003). Finally, Georgoulas et al. (2011) present some interesting results of CH<sub>4</sub> from space in the vicinity of the Mediterranean Sea, but only over land and essentially over the Eastern Mediterranean. The authors found, from the total columns of CH<sub>4</sub> as measured by SCIAMACHY in 2003 and 2004, an obvious maximum in August that could not be attributed to any volcano eruptions although this area hosts a significant number of geological formations that could potentially contribute to the total CH<sub>4</sub> burden. Being given that the sensitivity of the SCIAMACHY CH<sub>4</sub> total columns covers the vertical domain 1000–200 hPa from the vertical structure of the averaging kernels presented in Buchwitz et al. (2005), we note that (1) this maximum localized in August is consistent with our study, and (2) the impact of the AMA on the CH<sub>4</sub> fields in the mid-to-upper troposphere cannot be ruled out.

In order to analyse the climatological impact of the AMA onto the EMB, we have calculated (Fig. 8) the climatological 6-day back trajectories from the point at 33° N, 35° E located in the EMB (red filled circle on Fig. 8) based on the British Atmospheric Data Centre (BADC) trajectory service (<http://badc.nerc.ac.uk/community/trajectory/>) from 1 July to 31 August (summer convective period) from 2001 to 2010 every 12 h at five different pressure levels: 850 and 700 hPa (lower troposphere), 500 hPa (middle troposphere), and 300 and 200 hPa (upper troposphere). The BADC trajectories were derived from 40-year (ERA40) re-analysis (2.5° × 2.5° / pressure levels) produced by the European Centre for Medium-Range Weather Forecasts (ECMWF). The position

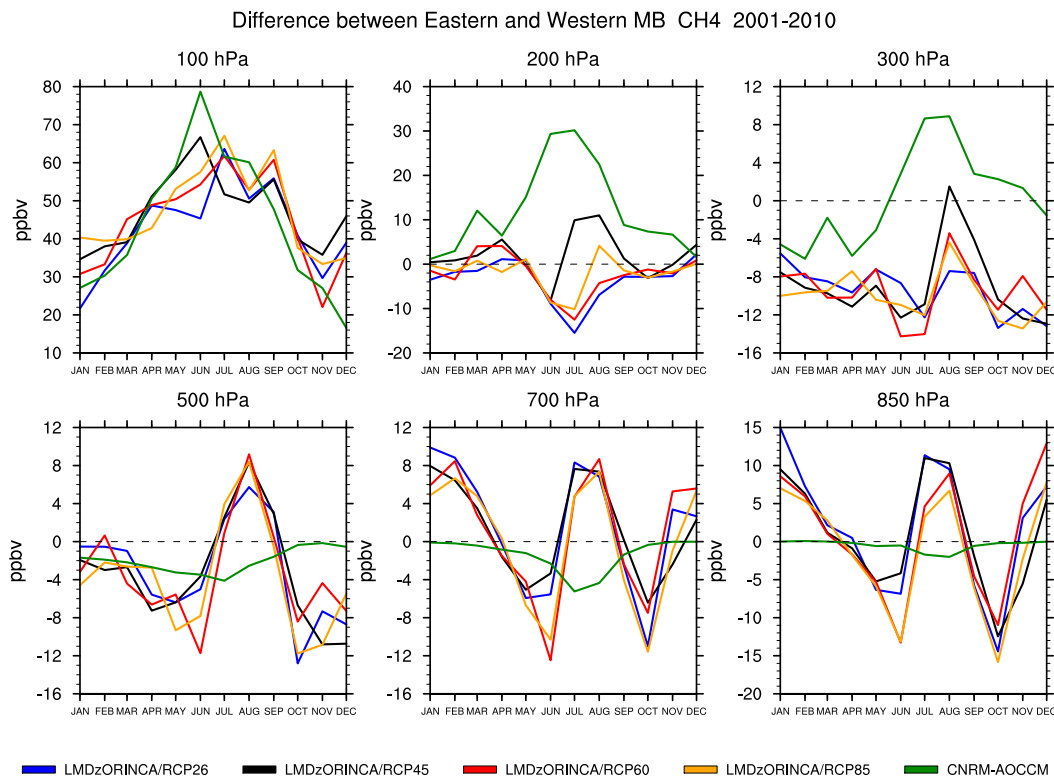


**Figure 9.** From top to bottom and from left to right: seasonal evolution of the difference in the CH<sub>4</sub> fields between the EMB and WMB over the climatological period 2001–2010 at 100, 200, 300, 500, 700 and 850 hPa as calculated by CNRM-AOCCM (green) model and LMDz-OR-INCA according to the four IPCC scenarios: RPCs 2.6 (blue), 4.5 (black), 6.0 (red) and 8.5 (yellow). See Sect. 2.2 for more details.

of the gravity centre of each distribution (i.e. the maximum in the probability distribution function) at each level is represented every 24 h by a star on Fig. 8. This methodology has been firstly used over the Dome C (Concordia) station in Antarctica (Ricaud, 2014). We have also performed the same analysis but for the winter period from 1 January to 31 March 2001–2010 (Fig. 8). Figure 8 undoubtedly shows that air parcels above the EMB during the Asian monsoon period of July–August from 2001 to 2010 originate: (a) from Asia in the upper troposphere, (b) from Northern America and Northern Africa in the mid-troposphere and (c) from Europe in the low troposphere. The same figure also shows that in winter (and all other seasons but summer, not shown) air parcels above the EMB originate from the west (Europe, Atlantic Ocean, North America, Pacific Ocean) whatever the pressure level considered from 850 to 100 hPa.

We apply the same climatological approach based on the CNRM-AOCCM and LMDz-OR-INCA CH<sub>4</sub> model results over the period 2001–2010. We consider (Fig. 9) the E–W CH<sub>4</sub> seasonal evolution at pressure levels from the lowermost troposphere to the lowermost stratosphere (850, 700, 500, 300, 200 and 100 hPa) and different scenarios for LMDz-OR-INCA (RCPs 2.6, 4.5, 6.0 and 8.5) in order to check out whether the summer peak still persists. We also repre-

sent the fields of CH<sub>4</sub> as specified and/or calculated in the lowermost level (surface level) by CNRM-AOCCM and by LMDz-OR-INCA (four scenarios) in summer averaged over the climatological period 2001–2010 over a wide area covering the MB and the Asian continent in Fig. 10, whilst the CH<sub>4</sub> fields calculated at 200 hPa are shown in Fig. 11.

The E–W CH<sub>4</sub> seasonal variations from the two models (Fig. 9) behave distinctively in the entire troposphere, and agree very well in the lowermost stratosphere. In the lower troposphere (850 and 700 hPa), the E–W CH<sub>4</sub> seasonal evolution from LMDz-OR-INCA exhibits a strong semi-annual oscillation of  $\pm 10$ – $15$  ppbv peaking in winter and summer for the four RCPs whilst the evolution from the CNRM-AOCCM shows a weak annual oscillation of 4–5 ppbv amplitude, with a strong minimum in summer, namely out-of-phase relative to the LMDz-OR-INCA variation. In the middle troposphere at 500 hPa, the four LMDz-OR-INCA outputs exhibit a net maximum in August of  $\sim 8$  ppbv with minima ranging from  $-2$  to  $-12$  ppbv from October to June, whilst the output from CNRM-AOCCM again shows a strong minimum in summer of about  $-4$  ppbv. At this stage, it is important to recall that the two models are GCMs with an on-line chemistry. The emissions of CH<sub>4</sub> are time-, longitude- and latitude-dependent in

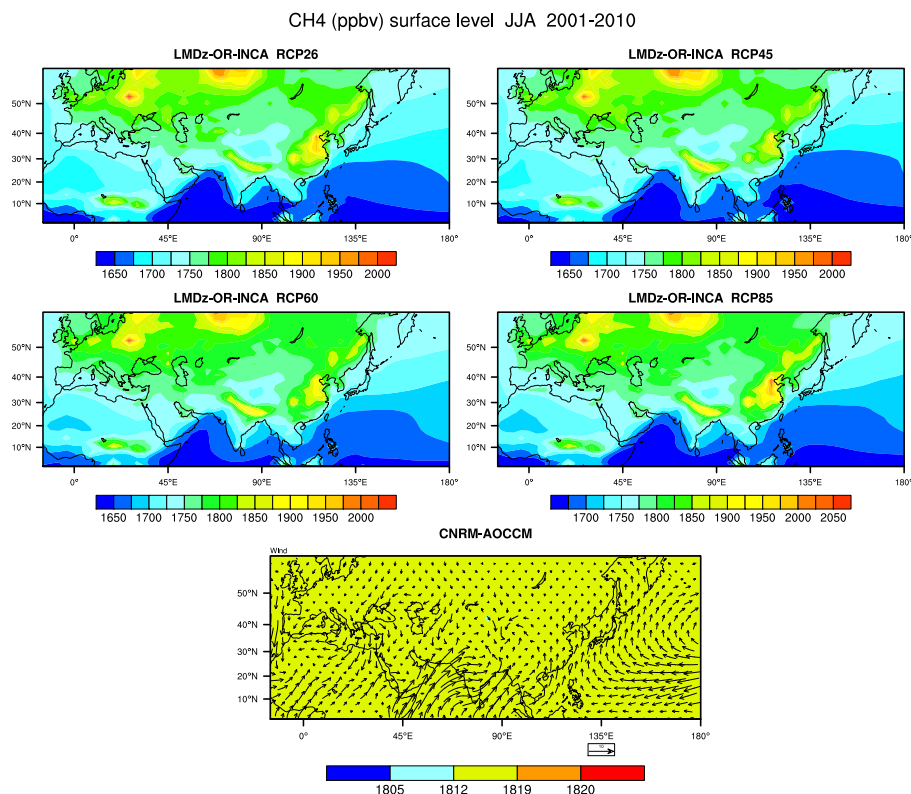


**Figure 10.** Fields of surface CH<sub>4</sub> as calculated by the CNRM-AOCCM model (bottom) and the LMDz-OR-INCA model (top and centre) according to the four IPCC scenarios (RCPs 2.6 (top left), 4.5 (top right), 6.0 (centre left) and 8.5 (centre right)) averaged over the summer season (JJA) and the climatological period 2001–2010. Superimposed to the CNRM-AOCCM CH<sub>4</sub> fields (bottom) is the wind field at the surface averaged over the same period. Note that the range of the colour scale changes for each figure and that the surface CH<sub>4</sub> for CNRM-AOCCM (bottom) is constant.

LMDz-OR-INCA with surface maxima over the northern continent (Fig. 10). In CNRM-AOCCM, there is no emission of CH<sub>4</sub> (Fig. 10) but mixing ratios of CH<sub>4</sub> between the surface and the 560 hPa level are relaxed towards evolving global mean surface abundances. This explains why the two models behave separately for pressures greater or equal to 500 hPa. Note that, regarding the shape of the E–W CH<sub>4</sub> seasonal evolution, there is no significant difference within the different scenarios of the LMDz-OR-INCA outputs since surface CH<sub>4</sub> shows the same structure independently of the RCPs considered (Fig. 10).

In the upper troposphere (200 and 300 hPa), the outputs from the two models show a peak in summer in the E–W CH<sub>4</sub> seasonal evolution (Fig. 9), but this differs from the RCPs considered for LMDz-OR-INCA. The maximum is much more intense in CNRM-AOCCM (~8 ppbv in July–August and ~30 ppbv in June–July at 300 and 200 hPa, respectively) than in LMDz-OR-INCA (~1 and ~10 ppbv in August for RCP 4.5 but only –4 and +4 ppbv in August for RCP 8.5 at 300 and 200 hPa, respectively; one peak at –4 ppbv in August for RCP 6.0 at 300 hPa but no peak at 200 hPa; no peak for RCP 2.6 neither at 300 nor at 200 hPa). On average, from

500 to 200 hPa, only the RCP 4.5 scenario from LMDz-OR-INCA shows a positive maximum in summer. At 300 and 200 hPa, the LMDz-OR-INCA summer peak is much less intense than the CNRM-AOCCM summer peak.

It is not obvious to understand why the E–W seasonal variation at 200 hPa is positive in summer for RCP 4.5 and not for the other RCPs (except RCP 8.5 in August). The horizontal distribution of CH<sub>4</sub> calculated by the two models at 200 hPa (Fig. 11) drastically differs but local maxima are centred within the AMA. A zonally symmetric structure showing a strong south–north gradient in CH<sub>4</sub> is modelled by CNRM-AOCCM with maxima in the tropics (1800 ppbv) and minima at high latitudes (1700 ppbv) and a local maximum centred within the core of the AMA with values greater than 1807 ppbv elongated towards two axis: (1) Southeast Asia and (2) Middle East and EMB. The CH<sub>4</sub> field calculated by LMDz-OR-INCA considering the four scenarios also shows two maxima over northern India and over Northeast Asia but the horizontal distribution is not zonally symmetric due to a zonally asymmetric CH<sub>4</sub> surface field. In all the scenarios considered, the CH<sub>4</sub> maxima within the AMA range from 1710 to 1750 ppbv with increasing RCPs from 2.6 to 8.5.



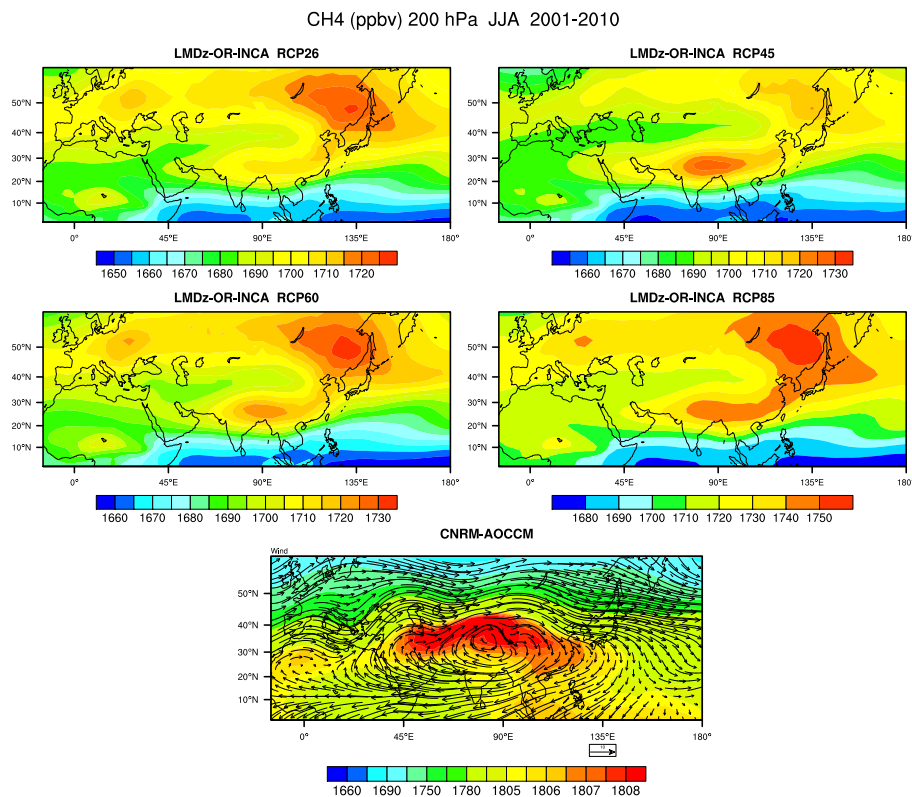


**Figure 11.** Fields of CH<sub>4</sub> as calculated by the CNRM-AOCCM model (bottom) and the LMDz-OR-INCA model (top and centre) considering the four IPCC scenarios (RCPs 2.6 (top left), 4.5 (top right), 6.0 (centre left) and 8.5 (centre right)) at 200 hPa averaged over the summer season (JJA) and the climatological period 2001–2010. Superimposed on the CNRM-AOCCM CH<sub>4</sub> fields (bottom) is the wind field at 200 hPa averaged over the same period. Note that the range of the colour scale changes for each figure and that the colour scale for the CNRM-AOCCM model (bottom) is nonlinear.

An elongated tongue of enriched CH<sub>4</sub> enters the EMB. More precisely, we can argue that in RCPs 2.6, 6.0 and 8.5, the primary maximum of CH<sub>4</sub> is located northward at 50° N, 135° E (CH<sub>4</sub> values greater than 1720, 1730 and 1750 ppbv, respectively) although it is a secondary maximum in RCP 4.5 (CH<sub>4</sub> values less than 1720 ppbv). Through long-range transport, this mid-latitude maximum is transported eastward within a band 40–50° N enriching CH<sub>4</sub> in the WMB and producing a E–W minimum in summer for RCPs 2.6, 6.0 and 8.5. Since there is a north–south gradient with a maximum in the south for CNRM-AOCCM, CH<sub>4</sub>-depleted air masses reach the WMB although CH<sub>4</sub>-enriched air masses from the AMA reach the EMB producing a systematic peak in summer, consistently with RCP 4.5.

In the lower stratosphere (100 hPa, Fig. 9), all the model outputs are consistent with each other showing an annual oscillation, with a wide maximum in summer (60–80 ppbv) and a wide minimum in winter (20–35 ppbv). This is apparently surprising keeping in mind that both models significantly differ from the surface (see Fig. 10) to ~500 hPa. But, in the WMB, the 100 hPa pressure corresponds to 420 K potential temperature both in summer (Fig. 2) and in winter (Fig. 4)

whilst, in the EMB, it corresponds to 390 K in summer and 400 K in winter, namely closer to the tropopause in summer than in winter. Consequently, whatever the model considered, the E–W CH<sub>4</sub> seasonal variation at 100 hPa (a) is always positive and (b) shows a peak in the summer period. We note that the summer peak in E–W seasonal evolution from the middle to the upper troposphere has also been observed and calculated by considering other constituents like CO and O<sub>3</sub> (not shown). This is the main topic of a forthcoming paper.

In conclusion, a schematic representation of the summertime processes impacting mid-to-upper CH<sub>4</sub> in the EMB is presented in Fig. 12. In our study, whatever the amount of CH<sub>4</sub> at the surface and its horizontal distribution, 1850–2000 ppbv for LMDz-OR-INCA consistently with the emission sources (Asia, Northern and Eastern Europe, Central Africa) or 1820 ppbv uniformly spread (Fig. 10), the Asian monsoon traps elevated amounts of CH<sub>4</sub> that converge through the depression, and are uplifted up to the upper troposphere at 200 hPa (Fig. 11) where they build up. At this level, the AMA re-distributes elevated amounts of CH<sub>4</sub> towards Middle East, North Africa and the EMB through

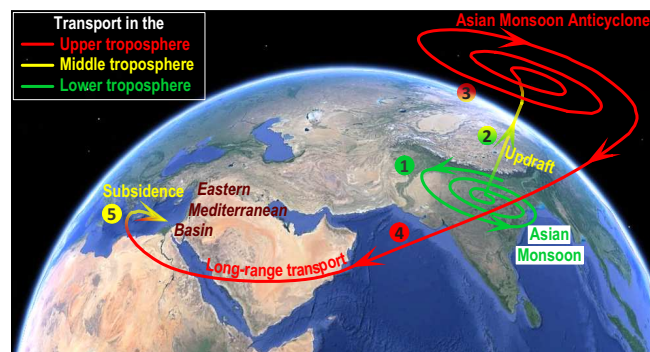


**Figure 12.** Schematic representation of the processes impacting the mid-to-upper tropospheric pollutants, including  $\text{CH}_4$ , above the EMB in summer (July–August). (1) Trapping of lower tropospheric pollutants in the Asian monsoon. (2) Updraft of pollutants in the Asian monsoon up to the upper troposphere. (3) Build-up of pollutants within the Asian monsoon in the upper troposphere. (4) Large-scale redistribution of pollutants by the Asian Monsoon Anticyclone to the Middle East and North Africa in the upper troposphere. (5) Build-up of pollutants through descent down to the middle troposphere above the EMB.

long-range transport. Finally, elevated amounts of  $\text{CH}_4$  build up in the EMB where they descend to the middle troposphere.

## 6 Conclusions

The present study is part of the Chemical and Aerosol Mediterranean Experiment (ChArMEx) programme. The aim is to investigate the tropospheric  $\text{CH}_4$  time and space variations above the MB and to attribute the variability to differing synoptic and global scales depending on the season and the altitude layer considered. Since the analysis of the mid-to-upper tropospheric  $\text{CH}_4$  distribution from spaceborne sensors and model outputs is challenging, we have used a wide variety of data sets. (1) First are the spaceborne measurements from thermal infrared (TIR) instruments: the Thermal And Near infrared Sensor for carbon Observations – Fourier Transform Spectrometer (TANSO-FTS) instrument on the Greenhouse gases Observing SATellite (GOSAT) satellite, the Atmospheric InfraRed Spectrometer (AIRS) on the Aura platform and the Infrared Atmospheric Sounder Interferometer (IASI) instrument aboard the MetOp-A platform. (2) There are also the model results from the Chemical Transport Model (CTM) MOCAGE, and the two Chemical Climate Models (CCMs) CNRM-AOCCM and LMDz-OR-INCA (the later considering different emission scenarios, RCPs 2.6, 4.5, 6.0 and 8.5).

Since  $\text{CH}_4$  is a long-lived tracer with lifetime of  $\sim 12$  years and is supposed to be well mixed in the troposphere, we had to adopt a climatological approach to highlight the weak expected variability. Spaceborne measurements and

the model results were selected and monthly averaged only over the Mediterranean Sea. The period under interest spans from 2008 to 2011 for the satellite measurements and the MOCAGE model results whilst, regarding the CCMs, we have averaged the model outputs over the climatological period from 2001 to 2010.

From both satellite and model results, our study obviously demonstrates the persistence of an east–west gradient in  $\text{CH}_4$  from the middle to the upper troposphere with a maximum in the WMB whatever the season considered except in summer when larger amounts of  $\text{CH}_4$  accumulate above the EMB. In winter, air masses mainly originating from Atlantic Ocean and Europe tend to favour an elevated amount of mid-to-upper tropospheric  $\text{CH}_4$  in the west compared to the east of the MB, with a general upward transport above the MB. In summer, the meteorological condition of the MB is changed, favouring air from northern Africa and the Middle East together with the Atlantic Ocean and Europe, with a general descent above the EMB.

Our analysis shows that, in the upper troposphere (300 hPa), the peak-to-peak amplitude of the east–west seasonal variation in  $\text{CH}_4$  above the MB is weak but almost twice greater in the satellite measurements ( $\sim 25$  ppbv) than in the model data ( $\sim 15$  ppbv). The maximum of  $\text{CH}_4$  in summer above the EMB can be explained by a series of dynamical processes only occurring in summer. The Asian monsoon traps and uplifts high amounts of  $\text{CH}_4$  to the upper troposphere where it builds up. The AMA redistributes these elevated  $\text{CH}_4$  amounts towards North Africa and the Middle East to finally reach and descend in the EMB. Consequently, the seasonal variation of the difference in  $\text{CH}_4$  between the EMB and the WMB shows a maximum in summer for pressures from 500 to 100 hPa considering both spaceborne measurements and model results whatever the emission scenarios used for the CCMs. But only the RCP 4.5 scenario gives systematically a positive summer peak whatever the pressure level considered, consistently with the measurements.

From this study, we conclude that  $\text{CH}_4$  in the mid-to-upper troposphere over the MB is mainly affected by long-range transport, particularly intense in summer from Asia. Conversely, in the lower troposphere, the  $\text{CH}_4$  variability is driven by the local sources of emission in the vicinity of the MB. Other constituents can also be affected by this summer mechanism, e.g.  $\text{O}_3$  and CO (not shown). In a forthcoming paper, the time evolution of the  $\text{CH}_4$ ,  $\text{O}_3$  and CO fields above the MB and at the Asian scale is studied by considering the outputs from different CCMs in the contemporary period (2000–2010) in order to study the future evolution of the chemical climate over the MB by 2100. Finally, despite the fact that IASI  $\text{CH}_4$  data as delivered by EUMETSAT are not operational, the seasonal variation of the east–west difference in  $\text{CH}_4$  total columns is nevertheless consistent with theoretical results and measurements from AIRS and IASI.

**Acknowledgements.** We would like to thank the following institutes and programme for funding our study: Centre National de la Recherche Scientifique-Institut National des Sciences de l'Univers/CNRS-INSU, Centre National des Etudes Spatiales/CNES, Agence de l'Environnement et de la Maîtrise de l'Energie/ADEME through the programme the Mediterranean Integrated STudies at Regional And Local Scales/MISTRALS Chemistry-Aerosol Mediterranean Experiment/ChArMEX. We also thank the following databases for allowing access to their data: the French database Ether, the European Organisation for the Exploitation of Meteorological Satellites, the GOSAT User Interface Gateway, the National Oceanic and Atmospheric Administration, the British Atmospheric Data Centre to access the LMDz-OR-INCA model data through the international Atmospheric Chemistry and Climate Model Intercomparison Project initiative, and the Global Atmosphere Watch from the World Meteorological Organization. We thank the British Atmospheric Data Centre, which is part of the Natural Environment Research Council (NERC) National Centre for Atmospheric Science (NCAS), for the calculation of trajectories and access to European Centre for Medium-Range Weather Forecasts (ECMWF) data. We finally would like to thank the two anonymous reviewers for their fruitful comments.

Edited by: C. Reeves

## References

- August, T., Klaes, D., Schlüssel, P., Hultberg, T., Crapeau, M., Ariaga, A., O'Carroll, A., Coppens, D., Munro, R., and Calbet, X.: IASI on Metop-A: Operational Level 2 retrievals after five years in orbit, *J. Quant. Spectrosc. Rad. Transfer*, 113, 1340–1371, 2012.
- Bergamaschi, P., Frankenberg, C., Fokke Meirink, J., Krol, M., Villani, M. G., Houweling, S., Dentener, F., Dlugokencky, E. J., Miller, J. B., Gatti, L. V., Engel, A., and Levin, I.: Inverse modeling of global and regional CH<sub>4</sub> emissions using SCIAMACHY satellite retrievals, *J. Geophys. Res.*, 114, D22301, doi:10.1029/2009JD012287, 2009.
- Bousquet, P., Ringeval, B., Pison, I., Dlugokencky, E. J., Brunke, E.-G., Carouge, C., Chevallier, F., Fortems-Cheiney, A., Frankenberg, C., Hauglustaine, D. A., Krummel, P. B., Langenfelds, R. L., Ramonet, M., Schmidt, M., Steele, L. P., Szopa, S., Yver, C., Viovy, N., and Ciais, P.: Source attribution of the changes in atmospheric methane for 2006–2008, *Atmos. Chem. Phys.*, 11, 3689–3700, doi:10.5194/acp-11-3689-2011, 2011.
- Buchwitz, M., Rozanov, V. V., and Burrows, J. P.: A near-infrared optimized DOAS method for the fast global retrieval of atmospheric CH<sub>4</sub>, CO, CO<sub>2</sub>, H<sub>2</sub>O, and N<sub>2</sub>O total column amounts from SCIAMACHY Envisat-1 nadir radiances, *J. Geophys. Res.*, 105, 15231–15245, doi:10.1029/2000JD900191, 2000.
- Buchwitz, M., de Beek, R., Burrows, J. P., Bovensmann, H., Warneke, T., Notholt, J., Meirink, J. F., Goede, A. P. H., Bergamaschi, P., Körner, S., Heimann, M., and Schulz, A.: Atmospheric methane and carbon dioxide from SCIAMACHY satellite data: initial comparison with chemistry and transport models, *Atmos. Chem. Phys.*, 5, 941–962, doi:10.5194/acp-5-941-2005, 2005.
- Christoudias, T., Pozzer, A., and Lelieveld, J.: Influence of the North Atlantic Oscillation on air pollution transport, *Atmos. Chem. Phys.*, 12, 869–877, doi:10.5194/acp-12-869-2012, 2012.
- Claeyman, M., Attié, J.-L., El Amraoui, L., Cariolle, D., Peuch, V.-H., Teyssède, H., Josse, B., Ricaud, P., Massart, S., Piacentini, A., Cammas, J.-P., Livesey, N. J., Pumphrey, H. C., and Edwards, D. P.: A linear CO chemistry parameterization in a chemistry-transport model: evaluation and application to data assimilation, *Atmos. Chem. Phys.*, 10, 6097–6115, doi:10.5194/acp-10-6097-2010, 2010.
- Claeyman, M., Attié, J.-L., Peuch, V.-H., El Amraoui, L., Lahoz, W. A., Josse, B., Ricaud, P., von Clarmann, T., Höpfner, M., Orphal, J., Flaud, J.-M., Edwards, D. P., Chance, K., Liu, X., Pasternak, F., and Cantié, R.: A geostationary thermal infrared sensor to monitor the lowermost troposphere: O<sub>3</sub> and CO retrieval studies, *Atmos. Meas. Tech.*, 4, 297–317, doi:10.5194/amt-4-297-2011, 2011.
- Clerbaux, C., Chazette, P., Hadji-Lazaro, J., Mégie, G., Müller, J.-F., and Clough, S. A.: Remote sensing of CO, CH<sub>4</sub>, and O<sub>3</sub> using a spaceborne nadir-viewing interferometer, *J. Geophys. Res.*, 103, 18999–19013, doi:10.1029/98JD01422, 1998.
- Courtier, P., Freydisier, C., Geleyn, J. F., Rabier, F., and Rochas, M.: The ARPEGE project at METEO-FRANCE, in: *Proc ECMWF Workshop. Numerical methods in atmospheric modelling*, 9–13 September 1991, 2, 193–231, ECMWF, Shinfield Park, Reading, UK, 1991.
- Crevoisier, C., Nobileau, D., Armante, R., Crépeau, L., Machida, T., Sawa, Y., Matsueda, H., Schuck, T., Thonat, T., Pernin, J., Scott, N. A., and Chédin, A.: The 2007–2011 evolution of tropical methane in the mid-troposphere as seen from space by MetOp-A/IASI, *Atmos. Chem. Phys.*, 13, 4279–4289, doi:10.5194/acp-13-4279-2013, 2013.
- Cristofanelli, P., Fierli, F., Marinoni, A., Calzolari, F., Duchi, R., Burkhart, J., Stohl, A., Maione, M., Arduini, J., and Bonasoni, P.: Influence of biomass burning and anthropogenic emissions on ozone, carbon monoxide and black carbon at the Mt. Cimone GAW-WMO global station (Italy, 2165 m a.s.l.), *Atmos. Chem. Phys.*, 13, 15–30, doi:10.5194/acp-13-15-2013, 2013.
- Cros, B., Durand, P., and Cachier, H.: An overview of the ESCOMPTE campaign, *Atmos. Res.*, 69, 241–279, 2004.
- Dayan, U.: Climatology of Back Trajectories from Israel Based on Synoptic Analysis, *J. Climate Appl. Meteor.*, 25, 591–595, 1986.
- Dentener, F., Stevenson, D., Cofala, J., Mechler, R., Amann, M., Bergamaschi, P., Raes, F., and Derwent, R.: The impact of air pollutant and methane emission controls on tropospheric ozone and radiative forcing: CTM calculations for the period 1990–2030, *Atmos. Chem. Phys.*, 5, 1731–1755, doi:10.5194/acp-5-1731-2005, 2005.
- Drori, R., Dayan, U., Edwards, D. P., Emmons, L. K., and Erlick, C.: Attributing and quantifying carbon monoxide sources affecting the Eastern Mediterranean: a combined satellite, modelling, and synoptic analysis study, *Atmos. Chem. Phys.*, 12, 1067–1082, doi:10.5194/acp-12-1067-2012, 2012.
- Dufour, A., Amodei, M., Ancellet, G., and Peuch, V.-H.: Observed and modelled “chemical weather” during ESCOMPTE, *Atmos. Res.*, 74, 161–189, 2005.
- El Amraoui, L., Attié, J.-L., Semane, N., Claeyman, M., Peuch, V.-H., Warner, J., Ricaud, P., Cammas, J.-P., Piacentini, A., Cariolle, D., Massart, S., and Bencherif, H.: Midlatitude stratosphere – tro-

- posphere exchange as diagnosed by MLS O<sub>3</sub> and MOPITT CO assimilated fields, *Atmos. Chem. Phys.*, 10, 2175–2194, 2010, <http://www.atmos-chem-phys.net/10/2175/2010/>.
- EUMETSAT, IASI Level 2 Products Guide, EUM/OPS-EPS/MAN/04/0033, available at: <http://oiswww.eumetsat.org/WEBOPS/eps-pg/IASI-L2/IASIL2-PG-0TOC.htm> (last access: 27 October 2014), 2004.
- Folberth, G. A., Hauglustaine, D. A., Lathière, J., and Brocheton, F.: Interactive chemistry in the Laboratoire de Météorologie Dynamique general circulation model: model description and impact analysis of biogenic hydrocarbons on tropospheric chemistry, *Atmos. Chem. Phys.*, 6, 2273–2319, doi:10.5194/acp-6-2273-2006, 2006.
- Georgoulas, A. K., Kourtidis, K. A., Buchwitz, M., Schneising, O., and Burrows, J. P.: A case study on the application of SCIAMACHY satellite methane measurements for regional studies: the Greater Area of Eastern Mediterranean, *Int. J. Remote Sens.*, 32, 787–813, doi:10.1080/01431161.2010.517791, 2011.
- Giorgi, F. and Lionello, P.: Climate change projections for the Mediterranean region, *Global and Planetary Change*, 63, 90–104, doi:10.1016/j.gloplacha.2007.09.005, 2008.
- Hauglustaine, D. A., Hourdin, F., Jourdain, L., Filiberti, M.-A., Walters, S., Lamarque, J.-F., and Holland, E. A.: Interactive chemistry in the Laboratoire de Meteorologie Dynamique general circulation model: description and background tropospheric chemistry evaluation, *J. Geophys. Res.*, 109, D04314, doi:10.1029/2003JD003957, 2004.
- Hilton, F., Armante, R., August, T., Barnet, C., Bouchard, A., Camy-Peyret, C., Capelle, V., Clarisse, L., Clerbaux, C., Coheur, P.-F., Collard, A., Crevoisier, C., Dufour, G., Edwards, D., Faijan, F., Fourrié, N., Gambacorta, A., Goldberg, M., Guidard, V., Hurtmans, D., Illingworth, S., Jacquinet-Husson, N., Kerzenmacher, T., Klaes, D., Lavanant, L., Masiello, G., Matricardi, M., McNally, A., Newman, S., Pavelin, E., Payan, S., Péquignot, E., Peyridieu, S., Phulpin, T., Remedios, J., Schlüssel, P., Serio, C., Strow, L., Stubenrauch, C., Taylor, J., Tobin, D., Wolf, W., and Zhou, D.: Hyperspectral Earth Observation from IASI: Five Years of Accomplishments, *B. Am. Meteor. Soc.*, 93, 347–370, doi:10.1175/BAMS-D-11-00027.1, 2012.
- Hourdin, F., Musat, I., Bony, S., Braconnot, P., Codron, F., Dufresne, J.-L., Fairhead, L., Filiberti, M.-A., Friedlingstein, P., Grandpeix, J.-Y., Krinner, G., LeVan, P., Li, Z.-X., and Lott, F.: The LMDZ4 general circulation model: climate performance and sensitivity to parametrized physics with emphasis on tropical convection, *Clim. Dyn.*, 27, 787–813, doi:10.1007/s00382-006-0158-0, 2006.
- Huszar, P., Teyssède, H., Michou, M., Voldoire, A., Oliivié, D. J. L., Saint-Martin, D., Cariolle, D., Senesi, S., Salas Y Melia, D., Alias, A., Karcher, F., Ricaud, P., and Halenka, T.: Modeling the present and future impact of aviation on climate: an AOGCM approach with online coupled chemistry, *Atmos. Chem. Phys.*, 13, 10027–10048, doi:10.5194/acp-13-10027-2013, 2013.
- Im, U. and Kanakidou, M.: Impacts of East Mediterranean megacity emissions on air quality, *Atmos. Chem. Phys.*, 12, 6335–6355, doi:10.5194/acp-12-6335-2012, 2012.
- Imasu, R., Saitoh, N., and Niwa, Y.: Retrieval performance of GOSAT thermal infrared FTS sensor for measuring CO<sub>2</sub> concentrations, *Proc. SPIE 6744, Sensors, Systems, and Next-Generation Satellites XI*, 67440F, doi:10.1117/12.737796, 2007.
- IPCC: Climate change 2007: The physical science basis. Contribution of working group I to the fourth assessment report of the intergovernmental panel on climate change, Cambridge, UK and New York, USA, Cambridge University Press, 996 pp., 2007.
- Josse, B., Simon, P., and Peuch, V.-H.: Rn–222 global simulations with the multiscale CTM MOCAGE, *Tellus*, 56B, 339–356, 2004.
- Kallos, G., Astitha, M., Katsafados, P., and Spyrou, C.: Long-Range Transport of Anthropogenically and Naturally Produced Particulate Matter in the Mediterranean and North Atlantic: Current State of Knowledge, *J. Appl. Meteorol. Clim.*, 46, 1230–1251, 2007.
- Kanakidou, M., Mihalopoulos, N., Kindap, T., Im, U., Vrekousis, M., Gerasopoulos, E., Dermizaki, E., Unal, A., Kocak, M., Markakis, K., Melas, D., Kouvarakis, G., Youssef, A. F., Richter, A., Hatzianastassiou, N., Hilboll, A., Ebojie, F., von Savigny, C., Ladstaetter-Weissenmayer, A., Burrows, J., and Moubasher, H.: Megacities as hot spots of air pollution in the East Mediterranean, *Atmos. Environ.*, 45, 1223–1235, 2011.
- Krinner, G., Viovy, N., de Noblet-Ducoudré, N., Ogée, J., Polcher, J., Friedlingstein, P., Ciais, P., Sitch, S., and Prentice, I. C.: A dynamic global vegetation model for studies of the coupled atmosphere-biosphere system, *Global Biogeochem. Cy.*, 19, GB1015, doi:10.1029/2003GB002199, 2005.
- Kuze, A., Suto, H., Nakajima, M., and Hamazaki, T.: Thermal and near infrared sensor for carbon observation Fourier-transform spectrometer on the Greenhouse Gases Observing Satellite for greenhouse gases monitoring, *Appl. Opt.*, 48, 6716–6733, 2009.
- Ladstätter-Weissenmayer, A., Heland, J., Kormann, R., von Kuhlmann, R., Lawrence, M. G., Meyer-Arne, J., Richter, A., Wittrock, F., Ziereis, H., and Burrows, J. P.: Transport and build-up of tropospheric trace gases during the MINOS campaign: comparison of GOME, in situ aircraft measurements and MATCH-MPIC-data, *Atmos. Chem. Phys.*, 3, 1887–1902, doi:10.5194/acp-3-1887-2003, 2003.
- Lamarque, J.-F., Kyle, G. P., Meinshausen, M., Riahi, K., Smith, S. J., van Vuuren, D. P., Conley, A. J., and Vitt, F.: Global and regional evolution of short-lived radiatively-active gases and aerosols in the Representative Concentration Pathways, *Climatic Change*, 109, 191–212, doi:10.1007/s10584-011-0155-0, 2011.
- Lamarque, J.-F., Shindell, D. T., Josse, B., Young, P. J., Cionni, I., Eyring, V., Bergmann, D., Cameron-Smith, P., Collins, W. J., Doherty, R., Dalsoren, S., Faluvegi, G., Folberth, G., Ghan, S. J., Horowitz, L. W., Lee, Y. H., MacKenzie, I. A., Nagashima, T., Naik, V., Plummer, D., Righi, M., Rumbold, S. T., Schulz, M., Skeie, R. B., Stevenson, D. S., Stroe, S., Sudo, K., Szopa, S., Voulgarakis, A., and Zeng, G.: The Atmospheric Chemistry and Climate Model Intercomparison Project (ACCMIP): overview and description of models, simulations and climate diagnostics, *Geosci. Model Dev.*, 6, 179–206, doi:10.5194/gmd-6-179-2013, 2013.
- Lefèvre, F., Brasseur, G. P., Folkins, I., Smith, A. K., and Simon, P.: Chemistry of the 1991–1992 stratospheric winter: Three-dimensional model simulations, *J. Geophys. Res.*, 99, 9183–9195, 1994.
- Lelieveld, J., Berresheim, H., Borrmann, S., Crutzen, P. J., Dentener, F. J., Fischer, H., Feichter, J., Flatau, P. J., Heland, J., Holzinger, R., Kormann, R., Lawrence, M. G., Levin, Z., Markowicz, K. M., Mihalopoulos, N., Minikin, A., Ramanathan,

- V., de Reus, M., Roelofs, G. J., Scheeren, H. A., Sciare, J., Schlager, H., Schultz, M., Siegmund, P., Steil, B., Stephanou, E. G., Stier, P., Traub, M., Warneke, C., Williams, J., and Ziereis, H.: Global Air Pollution Crossroads over the Mediterranean, *Science*, 298, 5594, 794–799, doi:10.1126/science.1075457, 2002.
- Lionello, P. (Ed.): The Climate of the Mediterranean Region: From the past to the future, 592 pp., Elsevier, ISBN978-0-12-416042-2, 2012.
- Liu, J. J., Jones, D. B. A., Worden, J. R., Noone, D., Parrington, M., and Kar, J.: Analysis of the summertime buildup of tropospheric ozone abundances over the Middle East and North Africa as observed by the Tropospheric Emission Spectrometer instrument, *J. Geophys. Res.*, 114, D05304, doi:10.1029/2008JD010993, 2009.
- Masson, O., Piga, D., Gurriaran, R., and D'Amico, D.: Impact of an exceptional Saharan dust outbreak in France: PM<sub>10</sub> and artificial radionuclides concentrations in air and in dust deposit, *Atmos. Env.*, 44, 20, 2478–2486, doi:10.1016/j.atmosenv.2010.03.004, 2010.
- Michou, M. and Peuch, V.-H.: Surface exchanges in the MOCAGE multiscale Chemistry and Transport Model, *J. Water Sci.*, 15, 173–203, 2002.
- Michou, M., Saint-Martin, D., Teyssèdre, H., Alias, A., Karcher, F., Oliu, D., Voldoire, A., Josse, B., Peuch, V.-H., Clark, H., Lee, J. N., and Chéroux, F.: A new version of the CNRM Chemistry-Climate Model, CNRM-CCM: description and improvements from the CCMVal-2 simulations, *Geosci. Model Dev.*, 4, 873–900, doi:10.5194/gmd-4-873-2011, 2011.
- Millán, M. M., Salvador, R., Mantilla, E., and Kallos, G.: Photooxidant dynamics in the Mediterranean basin in summer: Results from European research projects, *J. Geophys. Res.*, 102, 8811–8823, doi:10.1029/96JD03610, 1997.
- Nabat, P., Solmon, F., Mallet, M., Kok, J. F., and Somot, S.: Dust emission size distribution impact on aerosol budget and radiative forcing over the Mediterranean region: a regional climate model approach, *Atmos. Chem. Phys.*, 12, 10545–10567, doi:10.5194/acp-12-10545-2012, 2012.
- Naik, V., Voulgarakis, A., Fiore, A. M., Horowitz, L. W., Lamarque, J.-F., Lin, M., Prather, M. J., Young, P. J., Bergmann, D., Cameron-Smith, P. J., Cionni, I., Collins, W. J., Dalsøren, S. B., Doherty, R., Eyring, V., Faluvegi, G., Folberth, G. A., Josse, B., Lee, Y. H., MacKenzie, I. A., Nagashima, T., van Noije, T. P. C., Plummer, D. A., Righi, M., Rumbold, S. T., Skeie, R., Shindell, D. T., Stevenson, D. S., Strode, S., Sudo, K., Szopa, S., and Zeng, G.: Preindustrial to present-day changes in tropospheric hydroxyl radical and methane lifetime from the Atmospheric Chemistry and Climate Model Intercomparison Project (ACCMIP), *Atmos. Chem. Phys.*, 13, 5277–5298, doi:10.5194/acp-13-5277-2013, 2013.
- Park, M., Randel, W. J., Emmons, L. K., and Livesey, N. J.: Transport pathways of carbon monoxide in the Asian summer monsoon diagnosed from Model of Ozone and Related Tracers (MOZART), *J. Geophys. Res.*, 114, D08303, doi:10.1029/2008JD010621, 2009.
- Peuch, V.-H., Amodei, M., Barthet, T., Cathala, M.-L., Josse, B., Michou, M., and Simon, P.: MOCAGE: Modèle de Chimie, Atmosphérique A Grande Echelle, Actes des Atelier de Modélisation de l'Atmosphère, Météo-France, 33–36, 1999.
- Pfister, G., Pétron, G., Emmons, L. K., Gille, J. C., Edwards, D. P., Lamarque, J.-F., J.-L. Attié, C. Granier, and Novelli, P. C.: Evaluation of CO simulations and the analysis of the CO budget for Europe, *J. Geophys. Res.-Atmos.*, 109, D19304, doi:10.1029/2004JD004691, 2004.
- Randel, W. J. and Park, M.: Deep convective influence on the Asian summer monsoon anticyclone and associated tracer variability observed with Atmospheric Infrared Sounder (AIRS), *J. Geophys. Res.*, 111, D12314, doi:10.1029/2005JD006490, 2006.
- Razavi, A., Clerbaux, C., Wespes, C., Clarisse, L., Hurtmans, D., Payan, S., Camy-Peyret, C., and Coheur, P. F.: Characterization of methane retrievals from the IASI space-borne sounder, *Atmos. Chem. Phys.*, 9, 7889–7899, doi:10.5194/acp-9-7889-2009, 2009.
- Ricaud, P.: Variabilités de la vapeur d'eau et de la température troposphérique mesurées par le radiomètre micro-onde HAMSTRAD au Pôle C, Antarctique. Partie II: résultats scientifiques, *La Météorologie*, 85, 35–46, doi:10.4267/2042/53749, 2014.
- Ricaud, P., Attié, J.-L., Teyssèdre, H., El Amraoui, L., Peuch, V.-H., Matricardi, M., and Schluessel, P.: Equatorial total column of nitrous oxide as measured by IASI on MetOp-A: implications for transport processes, *Atmos. Chem. Phys.*, 9, 3947–3956, doi:10.5194/acp-9-3947-2009, 2009.
- Rodgers, C. D.: Inverse Methods for Atmospheric Sounding: Theory and Practice, 1st Ed., Singapore, World Scientific, 2000.
- Rodwell, M. J. and Hoskins, B. J.: Monsoons and the dynamics of deserts, *Q. J. R. Meteorol. Soc.*, 122, 1385–1404, 1996.
- Saitoh, N., Touno, M., Hayashida, S., Imasu, R., Shiomi, K., Yokota, T., Yoshida, Y., Machida, T., Matsueda, H., and Sawa, Y.: Comparisons between XCH<sub>4</sub> from GOSAT Shortwave and Thermal Infrared Spectra and Aircraft CH<sub>4</sub> Measurements over Guam, *SOLA*, 8, 145–149, doi:10.2151/sola.2012-036, 2012.
- Scheeren, H. A., Lelieveld, J., Roelofs, G. J., Williams, J., Fischer, H., de Reus, M., de Gouw, J. A., Warneke, C., Holzinger, R., Schlager, H., Klüpfel, T., Bolder, M., van der Veen, C., and Lawrence, M.: The impact of monsoon outflow from India and Southeast Asia in the upper troposphere over the eastern Mediterranean, *Atmos. Chem. Phys.*, 3, 1589–1608, doi:10.5194/acp-3-1589-2003, 2003.
- Schicker, I., Radanovics, S., and Seibert, P.: Origin and transport of Mediterranean moisture and air, *Atmos. Chem. Phys.*, 10, 5089–5105, doi:10.5194/acp-10-5089-2010, 2010.
- Schlüssel, P., Hultberg, T. H., Phillips, P. L., August, T., and Calbet, X.: The operational IASI Level 2 Processor, *Adv. Space Res.*, 36, 982–988, 2005.
- Stockwell, W. R., Kirchner, F., Kuhn, M., and Seefeld, S.: A new mechanism for regional atmospheric chemistry modelling, *J. Geophys. Res. Atmos.*, 102, 25847–25879, 1997.
- Susskind, J., Blaisdell, J. M., Iredell, L. and Keita, F.: Improved Temperature Sounding and Quality Control Methodology Using AIRS/AMSU Data: The AIRS Science Team Version 5 Retrieval Algorithm, *IEEE Trans. Geosci. Remote Sens.*, 49, 883–907, 2011.
- Szopa, S., Balkanski, Y., Schulz, M., Bekki, S., Cugnet, D., Fortems-Cheiney, A., Turquety, S., Cozic, A., Déandres, C., Hauglustaine, D., Idelkadi, A., Lathière, J., Lefèvre, F., Marchand, M., Vuolo, R., Yan, N., and Dufresne, J.-L.: Aerosol and ozone changes as forcing for climate evolution between 1850 and 2100, *Clim. Dynam.*, 40, 2223–2250, doi:10.1007/s00382-012-1408-y, 2013.

- Turquety, S., Hadji-Lazaro, J., Clerbaux, C., Hauglustaine, D. A., Clough, S. A., Cassé, V., Schlüssel, P., and Mégie, G.: Operational trace gas retrieval algorithm for the Infrared Atmospheric Sounding Interferometer, *J. Geophys. Res.*, 109, D21301, doi:10.1029/2004JD004821, 2004.
- van der Werf, G. R., Randerson, J. T., Collatz, G. J., and Giglio, L.: Carbon emissions from fires in tropical and subtropical ecosystems, *Global Change Biol.*, 9, 547–562, 2003.
- Volz, A., Sanchez-Gomez, E., Salas y Melia, D., Decharme, B., Cassou, C., Sény, S., Valcke, S., Beau, I., Alias, A., Chevalier, M., Deque, M., Deshayes, J., Douville, H., Fernandez, E., Madec, G., Maisonnave, E., Moine, M.-P., Planton, S., Saint-Martin, D., Szopa, S., Tyteca, S., Alkama, R., Belamari, S., Braun, A., Coquart, L., and Chauvin, F.: The CNRM-CM5. 1 global climate model: description and basic evaluation, *Clim. Dynam.*, 40, 2091–2121, 2013.
- Voulgarakis, A., Naik, V., Lamarque, J.-F., Shindell, D. T., Young, P. J., Prather, M. J., Wild, O., Field, R. D., Bergmann, D., Cameron-Smith, P., Cionni, I., Collins, W. J., Dalsøren, S. B., Doherty, R. M., Eyring, V., Faluvegi, G., Folberth, G. A., Horowitz, L. W., Josse, B., MacKenzie, I. A., Nagashima, T., Plummer, D. A., Righi, M., Rumbold, S. T., Stevenson, D. S., Strode, S. A., Sudo, K., Szopa, S., and Zeng, G.: Analysis of present day and future OH and methane lifetime in the ACCMIP simulations, *Atmos. Chem. Phys.*, 13, 2563–2587, doi:10.5194/acp-13-2563-2013, 2013.
- Wanger, A., Peleg, M., Sharf, G., Mahrer, Y., Dayan, U., Kallos, G., Kotroni, V., Lagouvardos, K., Varinou, M., Papadopoulos, A., and Luria, M.: Some Observational and Modelling Evidence of Long Range Transport of Air Pollutants from Europe Towards the Israeli Coast, *J. Geophys. Res.*, 105, 7177–7186, 2000.
- Worden, J., Kulawik, S., Frankenberg, C., Payne, V., Bowman, K., Cady-Peirara, K., Wecht, K., Lee, J.-E., and Noone, D.: Profiles of CH<sub>4</sub>, HDO, H<sub>2</sub>O, and N<sub>2</sub>O with improved lower tropospheric vertical resolution from Aura TES radiances, *Atmos. Meas. Tech.*, 5, 397–411, doi:10.5194/amt-5-397-2012, 2012.
- Wunch, D., Toon, G. C., Wennberg, P. O., Wofsy, S. C., Stephens, B. B., Fischer, M. L., Uchino, O., Abshire, J. B., Bernath, P., Biraud, S. C., Blavier, J.-F. L., Boone, C., Bowman, K. P., Browell, E. V., Campos, T., Connor, B. J., Daube, B. C., Deutscher, N. M., Diao, M., Elkins, J. W., Gerbig, C., Gottlieb, E., Griffith, D. W. T., Hurst, D. F., Jiménez, R., Keppel-Aleks, G., Kort, E. A., Macatangay, R., Machida, T., Matsueda, H., Moore, F., Morino, I., Park, S., Robinson, J., Roehl, C. M., Sawa, Y., Sherlock, V., Sweeney, C., Tanaka, T., and Zondlo, M. A.: Calibration of the Total Carbon Column Observing Network using aircraft profile data, *Atmos. Meas. Tech.*, 3, 1351–1362, doi:10.5194/amt-3-1351-2010, 2010.
- Xiong, X., Barnett, C., Maddy, E., Sweeney, C., Liu, X., Zhou, L., and Goldberg, M.: Characterization and validation of methane products from the Atmospheric Infrared Sounder (AIRS), *J. Geophys. Res.*, 113, G00A01, doi:10.1029/2007JG000500, 2008.
- Yokota, T., Yoshida, Y., Eguchi, N., Ota, Y., Tanaka, T., Watanabe, H., and Maksyutov, S.: Global Concentrations of CO<sub>2</sub> and CH<sub>4</sub> Retrieved from GOSAT: First Preliminary Results, *SOLA*, 5, 160–163, doi:10.2151/sola.2009-041, 2009.
- Yoshida, Y., Kikuchi, N., Morino, I., Uchino, O., Oshchepkov, S., Bril, A., Saeki, T., Schutgens, N., Toon, G. C., Wunch, D., Roehl, C. M., Wennberg, P. O., Griffith, D. W. T., Deutscher, N. M., Warneke, T., Notholt, J., Robinson, J., Sherlock, V., Connor, B., Rettinger, M., Sussmann, R., Ahonen, P., Heikkinen, P., Kyrö, E., Mendonça, J., Strong, K., Hase, F., Dohe, S., and Yokota, T.: Improvement of the retrieval algorithm for GOSAT SWIR XCO<sub>2</sub> and XCH<sub>4</sub> and their validation using TCCON data, *Atmos. Meas. Tech.*, 6, 1533–1547, doi:10.5194/amt-6-1533-2013, 2013.
- Ziv, B., Saaroni, H., and Alpert, P.: The factors governing the summer regime of the eastern Mediterranean, *Int. J. Climatol.*, 24, 1859–1871, doi:10.1002/joc.1113, 2004.